

1  
2  
3  
4  
5  
6  
7  
8  
9  
10  
11  
12  
13  
14  
15  
16  
17  
18  
19  
20  
21  
22  
23  
24  
25  
26  
27  
28  
29  
30  
31  
32  
33  
34  
35  
36  
37  
38  
39  
40  
41  
42  
43  
44  
45  
46  
47  
48  
49  
50  
51  
52  
53  
54  
55  
56  
57  
58  
59  
60

**Environmental Significance Statement**

View Article Online  
DOI: 10.1039/D0EN00412J

In environmental systems, the production of iron-organic matter (Fe-OM) nano-aggregates has been significantly increasing in recent decades due to climate change. These nano-aggregates are expected to be a major controlling factor of micro-pollutant mobility. Herein, we demonstrate that with an increasing Ca concentration, Fe-OM structures move from nanometric aggregates to a micrometric network in which the size of Fe phases increases. These results shed new light on the mobility of Fe-OM aggregates and potentially associated micro-pollutants that seems to depend on Fe-OM organization which is modified by major ion species present during their production. These findings are of major importance to discern the structure and behaviour of Fe-OM colloids in their production areas such as riparian wetlands, soil erosions or permafrost thawing.

Environmental Science: Nano Accepted Manuscript

# How does calcium drive the structural organization of iron-organic matter aggregates?

## A multiscale investigation

Anthony Beauvois<sup>\*a,b,c</sup>, Delphine Vantelon<sup>b</sup>, Jacques Jestin<sup>c</sup>, Camille Rivard<sup>b,d</sup>,  
Martine Bouhnik-Le Coz<sup>a</sup>, Aurélien Dupont<sup>e</sup>, Valérie Briois<sup>b</sup>, Thomas Bizien<sup>b</sup>,  
Andrea Sorrentino<sup>f</sup>, Baohu Wu<sup>g</sup>, Marie-Sousai Appavou<sup>g</sup>, Elaheh Lotfi-  
Kalahroodi<sup>a</sup>, Anne-Catherine Pierson-Wickmann<sup>a</sup> and Mélanie Davranche<sup>a</sup>

<sup>a</sup>Univ. Rennes, CNRS, Géosciences Rennes - UMR 6118, F-35000 Rennes, France

<sup>b</sup>Synchrotron SOLEIL, L'Orme des Merisiers, Saint-Aubin BP48, 91192 Gif-sur-Yvette Cedex

<sup>c</sup>Laboratoire Léon Brillouin, CEA Saclay, 91191 Gif-sur-Yvette Cedex

<sup>d</sup>INRAE - UAR 1008 TRANSFORM, F-44316 Nantes, France

<sup>e</sup>Univ Rennes, CNRS, Inserm, BIOSIT - UMS 3480, US\_S 018, F-35000 Rennes, France

<sup>f</sup>ALBA Synchrotron Light Facility, Carrer de la Llum 2-26, 08290 Cerdanyola del Vallès, Spain

<sup>g</sup>Forschungszentrum Jülich, JCNS am MLZ, Lichtenbergstr. 1, 85748 Garching, Germany

<sup>\*</sup>Corresponding author: [anthony.beauvois@univ-rennes1.fr](mailto:anthony.beauvois@univ-rennes1.fr)

### **Abstract**

Iron-organic matter (Fe-OM) aggregates are a key factor in the control of pollutant mobility. Their physical and structural organization depends on the prevailing physicochemical

1  
2  
3  
4  
5  
6  
7  
8  
9  
10  
11  
12  
13  
14  
15  
16  
17  
18  
19  
20  
21  
22  
23  
24  
25  
26  
27  
28  
29  
30  
31  
32  
33  
34  
35  
36  
37  
38  
39  
40  
41  
42  
43  
44  
45  
46  
47  
48  
49  
50  
51  
52  
53  
54  
55  
56  
57  
58  
59  
60

conditions during their formation and on subsequent exposure to variations in porewater geochemistry. Among these conditions, calcium (Ca) could be a major parameter given its high concentrations in the environment and its affinity for OM. Mimetic environmental Fe-OM-Ca associations were synthesized at various Fe/organic carbon (OC) and Ca/Fe molar ratios using Leonardite humic acid as OM model. The impact of Ca on Fe-OM aggregates was studied by a combination of X-ray absorption spectroscopy, small angle X-ray and neutron scattering and imaging techniques (TEM, cryo-TEM and cryo-TXM). Iron phases are constituted of Fe(III)-oligomers, Fe(III)-nanoparticles and ferrihydrite (Fh), all bound or embedded by OM. Iron phases exhibit a fractal organization with Fe-primary beads aggregated as Fe-primary aggregates (Fe-PA) which themselves are embedded in an OM aggregates. For Ca/OC (mol/mol) < 0.026, Fe-PA aggregate in a third level as a Fe-secondary aggregate. For Ca/OC ≥ 0.026, OM forms a large Ca-branched network in which Ca is bound as a dimer to OM carboxylic sites. In such conditions, Fe-PA are distributed in the OM network, distant from each other. All these structural transitions are driven by Ca which partially screens the Fe-OM interactions. The formation of such micrometric network should impact both the surface reactivity of the Fe phases as well as the mobility of Fe, OM and associated elements, notably in the soil porosity where they are produced under natural conditions.

View Article Online  
DOI: 10.1039/D0EN00412J

Environmental Science: Nano Accepted Manuscript

## Introduction

View Article Online  
DOI: 10.1039/D0EN00412J

Environmental nanoparticles are ubiquitous in natural systems<sup>1</sup>. Among them, natural iron-organic matter (Fe-OM) aggregates are of major importance due to their high amounts in natural systems such as in wetlands<sup>2–4</sup>, peatlands<sup>5,6</sup> or permafrosts<sup>7,8</sup>. They are mainly produced in soils via anthropogenic forcing and geochemical and physical processes such as alteration and erosion, oxidation-reduction variations occurrence subsequent to soil water-saturation/desaturation alternation. The production of these aggregates has tended to strongly increase in recent decades due to global warming which result in an increase in rainfall frequency, volume and intensity as well as permafrost thawing. Due to their nanometric size and their high specific surface area, they are known to be a key factor in the mobility of metals and metalloids in environmental systems<sup>1,2,6,9,10</sup>. Their ability to adsorb metal(loid)s depends on the size, morphology and structural arrangement between the Fe and OM phases<sup>11,12</sup>. Several studies have investigated the structural organization of Fe phases formed during Fe(II) oxidation-hydrolysis or Fe(III) hydrolysis in the presence of OM<sup>13–18</sup>. Irrespective of the process of formation, the Fe speciation depends on the Fe/organic carbon (OC) ratio. For very low Fe/OC ratios, the dominant Fe species are Fe(III) oligomers bound to OM<sup>11,19</sup> while for high Fe/OC ratio, nanoparticulate Fe embedded in an OM matrix are formed<sup>20,21</sup>. For intermediate Fe/OC ratios, Fe-OM aggregates contain two distinct Fe phases: Fe(III) oligomers bound to OM and nano-sized ferrihydrite (Fh) embedded in an OM matrix<sup>14,18,22</sup>. According to Chen *et al.*<sup>18</sup>, a decrease in Fe(III) oligomers occurs to the benefit of Fh with an increasing Fe/OC ratio. Guénet *et al.*<sup>13</sup> demonstrated that the Fe part is organized according to a fractal network composed of Fe primary beads (radius  $\approx 0.8$  nm) that associate to form Fe primary aggregates (radius  $\approx 5$  nm) that are themselves associated as Fe secondary aggregates (radius  $> 100$  nm). They described the OM part as a compact aggregate (radius  $\approx 90$  nm) bound to Fe

secondary aggregates as well as isolated molecules bound to Fe primary aggregates. The size of Fe-OM aggregates increases with the increasing Fe/OC ratio.

These species were also observed in organic soil as Fe monomers and Fe oxyhydroxides bound to OM<sup>22</sup> and in boreal rivers as nano-Fh and Fe-OM complexes<sup>23</sup>. Thomas Arrigo *et al.*<sup>6</sup> reported the presence of lepidocrocite (Lp) and Fh in a peatland soil. Guénet *et al.*<sup>2</sup> studied a riparian wetland soil and provided evidence of the presence of nano-Lp embedded in an OM matrix, as well as small Fe clusters (i.e. oligomers) and Fe monomers bound to OM.

In the absence of OM, Fe(II) oxidation-hydrolysis leads to the formation of micrometric-sized aggregates of nano-Lp<sup>17,24</sup> whereas with humic acid (HA), Fe oxyhydroxides of nanometric size are formed<sup>2,14,17</sup>. Therefore, organic matter controls the behaviour of Fe in organic environments and the physical, chemical and morphological organization of Fe-OM aggregates is influenced by the prevailing physico-chemical conditions such as pH, ionic strength or other major cations<sup>25–27</sup>. In natural waters, calcium (Ca) is a major ion with a concentration ranging from  $1.0 \times 10^{-2}$  to  $1.0 \times 10^{-4}$  mol L<sup>-1</sup><sup>28</sup>. Several studies have investigated the impact of Ca on the structural organization of natural OM. Calcium acts as a coagulating agent for OM by forming cationic bridges between molecules, preferentially involving carboxylic groups<sup>29–31</sup> but also via phenolic groups with increasing pH values<sup>32</sup>. Kalinichev and Kirkpatrick<sup>31</sup> reported the formation of OM supramolecular structures with Ca. Calcium has also been shown to increase the adsorption of fulvic acids (FA) on goethite<sup>33</sup> leading to the formation of goethite-Ca-FA ternary associations, and to aggregate OM with clay minerals<sup>34</sup>. Adhikari *et al.*<sup>35</sup> provided evidence that the hydrolysis of Fe(III) with OM and Ca leads to the formation of Fh-OM-Ca precipitates in which OM acts as a bridge between Fh and Ca. Davis and Edwards<sup>36</sup> demonstrated that Ca<sup>2+</sup> complexation by OM enhances Fe(III) hydrolysis resulting in better polymerization of Fe with Ca. However, there are lacks of information on the overall structural organization of Fe-OM-Ca associations.

The aim of this study is therefore to provide a complete characterization of the impact of Ca on the composition and structural organization of Fe-OM aggregates. For this purpose, we synthesized Fe-OM-Ca associations with various Fe/OC and Ca/Fe ratios. Calcium interactions with Fe-OM and Fe speciation were investigated by X-ray absorption spectroscopy (XAS) at the Ca and Fe K-edge. The arrangement of nanoparticulate Fe and OM was probed combining small-angle X-rays scattering (SAXS), small-angle neutrons scattering (SANS) and very small-angle neutrons scattering (VSANS). The overall size of the aggregates was investigated by cryo-transmission X-ray microscopy (cryo-TXM) and cryo-transmission electron microscopy (cryo-TEM).

## **Experimental methods**

### **1. Sampling and chemical analyses**

#### **1.1. Laboratory syntheses**

All aqueous solutions were prepared with ultrapure water (Milli-Q-Integral®, Millipore). Samples were synthesized at three Fe/OC molar ratios (i.e. 0.02, 0.05 and 0.08) and at four Ca/Fe molar ratios (i.e. 0, 0.1, 0.5 and 1) following the procedure described by Guénet *et al.*<sup>13</sup>. Samples were labelled Fexx-Cayy, where Fexx and Cayy represent the Fe/OC and the Ca/Fe ratios, respectively. The OM used was Leonardite Humic Acid (HA) (International Humic Substances Society) with the elemental composition C = 63.81%, O = 31.27%, H = 3.70% and N = 1.23% (as a mass fraction). A  $1.79 \times 10^{-2}$  mol L<sup>-1</sup> iron(II) stock solution was prepared with FeCl<sub>2</sub>·4H<sub>2</sub>O (Sigma Aldrich). From this solution, three Fe(II)-Ca(II) stock solutions were prepared at [Ca] =  $2.50 \times 10^{-3}$  mol L<sup>-1</sup>,  $1.25 \times 10^{-2}$  mol L<sup>-1</sup> and  $2.50 \times 10^{-2}$  mol L<sup>-1</sup> with CaCl<sub>2</sub>·2H<sub>2</sub>O (Sigma Aldrich). Aggregates (Fe-OM-Ca) were synthesized using a titration of a HA suspension at [OC] =  $1.00 \times 10^{-1}$  mol L<sup>-1</sup> with the Fe(II)-Ca(II) solution at 0.05 mL min<sup>-1</sup> in  $5 \times 10^{-3}$  mol L<sup>-1</sup> of NaCl using an automated titrator (Titrino 794, Metrohm). The pH was kept constant

1  
2  
3  
4  
5  
6  
7  
8  
9  
10  
11  
12  
13  
14  
15  
16  
17  
18  
19  
20  
21  
22  
23  
24  
25  
26  
27  
28  
29  
30  
31  
32  
33  
34  
35  
36  
37  
38  
39  
40  
41  
42  
43  
44  
45  
46  
47  
48  
49  
50  
51  
52  
53  
54  
55  
56  
57  
58  
59  
60

at 6.5 with a 0.1 mol L<sup>-1</sup> NaOH solution using a second titrator (Titrino 794, Metrohm) at a set pH mode. The accuracy of the pH measurement was ± 0.04 pH units. A fraction of each sample was subjected to filtration at 0.2 µm (cellulose acetate membrane filter, Sartorius) and ultrafiltration at 30 kDa (Vivaspin VS2022, Sartorius). Each 0.2 µm filter was rinsed before use with ultrapure water and each 30 kDa ultrafiltration cell was rinsed 10 times with NaOH 0.1 mol L<sup>-1</sup> and two times with ultrapure water. Two samples were also prepared using the same protocol but without Fe at Ca concentrations of 1.00×10<sup>-4</sup> and 5.00×10<sup>-3</sup> mol L<sup>-1</sup>.

1.2. Chemical analyses

OC concentrations were determined using an organic carbon analyser (Shimadzu TOC-V CSH). The accuracy of the OC measurement was determined to be ±5% using a standard solution of potassium hydrogen phthalate (Sigma Aldrich). The Fe and Ca concentrations were measured by ICP-MS using an Agilent Technologies 7700x instrument at the University of Rennes 1. To eliminate OM, samples were pre-digested with 14.6 mol L<sup>-1</sup> HNO<sub>3</sub> and suprapure® 30% H<sub>2</sub>O<sub>2</sub> at 90°C and evaporated. The final concentrations of Fe, Ca, and OC are reported in Table 1 for the bulk and in Table SI 1 for the filtrates and ultrafiltrates.

Environmental Science: Nano Accepted Manuscript

Table 1 – Fe, Ca and OC concentrations. \*Theoretical values, n.d.: not determined. Exp: experimental. Theo: theoretical. The uncertainties were calculated from the triplicate.

Sample name	Fe (mmol L <sup>-1</sup> )	Ca (mmol L <sup>-1</sup> )	OC (mmol L <sup>-1</sup> )	Ca/Fe (mol/mol)		Fe/OC (mol/mol)		Ca/OC (mol/mol)
				Exp	Theo	Exp	Theo	Exp
Fe0.00-Ca_4	0*	0.10*	58.0*	-	-	n.d.	0.00	0.002
Fe0.00-Ca_200	0*	5.00*	58.0*	-	-	n.d.	0.00	0.091
Fe0.02-Ca0.0	1.21 ± 0.05	0.10 ± 0.01	56.3 ± 0.9	0.10	0.10	0.02	0.02	0.002
Fe0.02-Ca0.1	1.07 ± 0.09	0.22 ± 0.02	54.3 ± 1.0	0.09	0.10	0.02	0.02	0.004
Fe0.02-Ca0.5	1.20 ± 0.08	0.65 ± 0.04	57.7 ± 1.7	0.10	0.10	0.02	0.02	0.011
Fe0.02-Ca1.0	1.30 ± 0.03	1.28 ± 0.04	55.8 ± 0.2	0.11	0.10	0.02	0.02	0.023
Fe0.05-Ca0.0	2.98 ± 0.22	0.10 ± 0.01	55.5 ± 0.9	0.25	0.25	0.05	0.05	0.002
Fe0.05-Ca0.1	3.23 ± 0.08	0.40 ± 0.01	55.5 ± 0.1	0.27	0.25	0.06	0.05	0.007
Fe0.05-Ca0.5	2.80 ± 0.13	1.45 ± 0.06	55.5 ± 0.9	0.24	0.25	0.05	0.05	0.026
Fe0.05-Ca1.0	2.70 ± 0.12	2.80 ± 0.09	51.9 ± 2.8	0.24	0.25	0.05	0.05	0.054
Fe0.08-Ca0.0	4.75 ± 0.12	0.10 ± 0.01	61.6 ± 1.0	0.36	0.40	0.08	0.08	0.002
Fe0.08-Ca0.1	5.00 ± 0.07	0.60 ± 0.01	60.8 ± 0.3	0.38	0.40	0.08	0.08	0.010
Fe0.08-Ca0.5	4.79 ± 0.10	2.38 ± 0.07	55.2 ± 1.9	0.40	0.40	0.09	0.08	0.043
Fe0.08-Ca1.0	4.95 ± 0.06	4.73 ± 0.01	51.8 ± 1.1	0.44	0.40	0.10	0.08	0.091



2. *Structural characterizations*

View Article Online  
DOI: 10.1039/D0EN00412J

2.1. *XAS data acquisition and analysis*

A fraction of each sample was freeze dried (Freeze dryer Alpha 1-2 LD plus, Christ). The obtained powder was pressed into a 6 mm pellet mixed with cellulose (Merck). X-ray absorption spectroscopy (XAS) at the Ca K-edge was performed on the LUCIA<sup>37,38</sup> beamline at the SOLEIL synchrotron (Saint-Aubin, France). The fixed exit double-crystal monochromator was equipped with Si(111) crystals. Spectra were recorded in fluorescence mode using a 60 mm<sup>2</sup> mono-element silicon drift diode detector (Bruker). The energy was calibrated using the calcite reference for which the first inflection point was set to 4045 eV.

The Fe K-edge spectra were recorded on the ROCK<sup>39</sup> beamline at the SOLEIL synchrotron. A Si(111) channel-cut was used as the monochromator. Spectra were recorded in transmission mode using three ionization chambers (Ohyo Koken) filled with N<sub>2</sub>. The energy was calibrated using a Fe foil located between the 2<sup>nd</sup> and the 3<sup>rd</sup> ionization chambers and measured simultaneously with the samples. Calibration was done by setting the maximum of the first derivate of the Fe foil to 7112 eV. The spectra were acquired with the quick-EXAFS technology allowing measuring one spectrum every 1s. For each sample, a total of 1500 spectra were recorded and could be superimposed, suggesting no damage of the sample due to the beam. The final spectrum was obtained by averaging the 1500 spectra. The references used for further data analysis were Fh and Lp synthesized following the procedure described in Schwertmann and Cornell<sup>24</sup>.

All XAS data were processed using the Athena software<sup>40</sup> including the Autbk algorithm (Rbkb = 1, k-weight = 3). Normalized Ca spectra were obtained by fitting the pre-edge region with a linear function and the post-edge region with a quadratic polynomial function. The Fourier transforms of the k<sup>3</sup>-weighted extended X-ray absorption fine structure (EXAFS) spectra were calculated over a range of 2-10.5 Å<sup>-1</sup> using a Hanning apodization window (window parameter

1  
2  
3 = 1). Back Fourier filters were extracted over the R-range of 1.3-3.1 Å, using the same  
4 apozidation window shape. The EXAFS fittings were performed in the 1.3–3.6 Å distance range  
5  
6 with the Artemis<sup>40</sup> interface to IFEFFIT using least-squares refinements. The paths used to fit  
7  
8 the Ca K-edge EXAFS were calculated from Ca-acetate<sup>41</sup> and Ca-2-furancarboxylate<sup>42</sup> using  
9  
10 the FEFF6 algorithm included in the Artemis interface<sup>43,44</sup>. Normalized Fe spectra were  
11  
12 obtained by fitting the pre-edge region with a linear function and the post-edge region with a  
13  
14 quadratic polynomial function. The Fourier transforms of the  $k^3$ -weighted EXAFS spectra were  
15  
16 calculated over a range of 2-12.5 Å<sup>-1</sup> using a Hanning apodization window (window parameter  
17  
18 = 1). Back Fourier filters were extracted over the R-range of 1.15-4.1 Å, using the same  
19  
20 apodization window shape. The EXAFS data were analysed by linear combination fitting (LCF)  
21  
22 available in the Athena software on the range 3-12.5 Å<sup>-1</sup>; all component weights were forced  
23  
24 to be positive. The references used were Fh, Lp and three pure components extracted from the  
25  
26 *in situ* synthesis of Fe-OM aggregates by Vantelon *et al.*<sup>14</sup>, i.e. Fe(II), Fe(III)-oligomers and  
27  
28 Fe(III)-Np that correspond to Fe(III) nano-oxyhydroxides, all bound or embedded in a HA  
29  
30 matrix. The best LCF fit was determined for the minimum  $n$ -components for which the R-factor  
31  
32 was better than 10% of the fit with  $n+1$  components. As without any constraint the total LCF  
33  
34 weight for each sample was between 0.95 and 1.05, it was arbitrarily fixed to 1 to facilitate  
35  
36 comparisons between each sample.

## 2.2. SAXS data acquisition and analysis

37  
38 Small angle X-ray scattering measurements were performed on the SWING beamline at the  
39  
40 SOLEIL synchrotron. Two sample-to-detector distances (1 and 6 m) were used with a  
41  
42 wavelength of 1.03 Å. This setup allowed access to a momentum transfer  $q$  range of  $2.0 \times 10^{-3}$ -  
43  
44  $0.7 \text{ Å}^{-1}$ . Measurements were also performed on the XEUSS 2.0 spectrometer from Xenocs  
45  
46 (CEA-LIONS/LLB, Saclay, France). Two sample-to-detector distances (33 and 249 cm) were  
47  
48 used with a wavelength of 1.54 Å (Cu X-ray source). This setup allowed access to a momentum  
49  
50  
51  
52  
53  
54  
55  
56  
57  
58  
59  
60

transfer range of  $4.5 \times 10^{-3}$ – $0.5 \text{ \AA}^{-1}$ . Measurements were performed on the suspensions except for the three settled samples (Figure SI 1) for which the experiments were carried out on the precipitate. All scattering curves were rescaled as a function of the apparent concentration in the high  $q$  range.

The cluster fractal model described in Guénet *et al.*<sup>13</sup> was used to analyse the SAXS curves. For centrosymmetric nanoparticles dispersed in a continuous solvent, here water, the scattered intensity is described by the following equation (eq. 1):

$$I(q) = \phi \cdot V \cdot \Delta\rho^2 \cdot P(q) \cdot S(q) \quad (\text{eq. 1})$$

where  $\phi$  is the volume fraction,  $V$  is the volume of the scattered entities,  $\Delta\rho^2$  is the contrast term,  $P(q)$  is the form factor and  $S(q)$  is the structure factor. The model was established considering that the samples are composed of Fe spherical poly-dispersed primary beads (Fe-PB). Part of these PB is organized as Fe primary aggregates (Fe-PA) described by a form factor according to a finite number of PB and a fractal dimension. These Fe-PA self-assembled as a third aggregation level, i.e. the Fe secondary aggregates (Fe-SA).

### 2.3. SANS and VSANS acquisition and analysis

The neutron scattering length density (SLD) of  $\text{H}_2\text{O}$  is  $\text{SLD}_{\text{H}_2\text{O}} = -0.56 \times 10^{10} \text{ cm}^{-2}$  while  $\text{SLD}_{\text{D}_2\text{O}} = 6.4 \times 10^{10} \text{ cm}^{-2}$ . Considering  $\text{SLD}_{\text{OM}} = 1.18 \times 10^{10} \text{ cm}^{-2}$  and  $\text{SLD}_{\text{Fe}} = 6.05 \times 10^{10} \text{ cm}^{-2}$ <sup>13</sup>, Fe-Ca-OM aggregates were synthesized in  $\text{D}_2\text{O}$  to match the Fe contribution to the neutron scattering and to only characterize the OM part. We completed the SANS investigation with a second intermediate contrast at 50/50%  $\text{H}_2\text{O}/\text{D}_2\text{O}$  to see whether we can identify a local contribution of the OM scattering signal. Small-angle neutron scattering (SANS) experiments were performed on the PA20 beamline (LLB, Saclay, France). Three sample-to-detector distances (2, 8 and 18 m) were used with a wavelength of 6 Å. This setup allowed access to a momentum transfer range of  $2.1 \times 10^{-3}$ – $0.3 \text{ \AA}^{-1}$ . SANS measurements were also performed on KWS-2 diffractometers<sup>45</sup> operated by the Jülich Centre for Neutron Science (JCNS) at the Heinz Maier-

Leibnitz Zentrum (MLZ) in Garching, Germany. Using a sample-to-detector distance of 11 m and 7.6 m with a wavelength of 7 Å ( $\Delta\lambda/\lambda = 10\%$ ) and a sample-to-detector distance of 19.5 m with a wavelength of 10 Å ( $\Delta\lambda/\lambda = 10\%$ ): the q-range  $1.9 \times 10^{-3}$ – $4.5 \times 10^{-1}$  Å<sup>-1</sup> was covered. Very small-angle neutron scattering (VSANS) experiments were carried out with KWS-3 diffractometers<sup>46</sup> operated by the JCNS at the MLZ. Using a neutron wavelength of 12.8 Å with  $\Delta\lambda/\lambda = 17\%$  and a sample to detector distance of 0.51 m, 1.25 m and 9.2 m, a q-range from approximately  $2.1 \times 10^{-4}$ – $5.0 \times 10^{-2}$  Å<sup>-1</sup> was covered. Like for SAXS, SANS measurements were performed on suspensions except for the three settled samples (Figure SI 1) for which experiments were carried out on the precipitate. All scattering curves were rescaled to the apparent concentration in the high q range. Data were corrected and calibrated using the PasiNet and QtiKWS softwares.

SANS curves were fitted using the SasView software with the following Guinier-Porod equation<sup>47</sup> (eq. 2):

$$I(q) = \begin{cases} \frac{G}{q^s} \exp\left(\frac{-q^2 R_g^2}{3-s}\right) & \text{for } q < q_{\text{cut-off}} \\ \frac{D}{q^\alpha} & \text{for } q > q_{\text{cut-off}} \end{cases} \quad (\text{eq. 2})$$

where G and D are scaling factors for the Guinier and Porod domains respectively,  $R_g$  is the gyration radius that corresponds to a typical size of the system, s is a parameter illustrating the nonspherical form of the object ( $s = 0$  for a sphere,  $s = 1$  for rods and  $s = 2$  for lamellae) and  $\alpha$  is the slope of the curve related to the fractal dimension ( $D_f$ ) of the object. The  $q_{\text{cut-off}}$  defines the limit between the Guinier and the Porod regime.

#### 2.4. Imaging

For the TEM measurements, 5 µL of the samples were dropped on a copper grid with a lacy carbon coated film (Agar scientific, AGS166-3) and then dried at room temperature. Transmission electron microscopy images were recorded using a JEOLL 100CXII instrument at 100 kV (THEMIS Analytical Facility, University of Rennes 1) equipped with an X-ray

1  
2  
3  
4  
5  
6  
7  
8  
9  
10  
11  
12  
13  
14  
15  
16  
17  
18  
19  
20  
21  
22  
23  
24  
25  
26  
27  
28  
29  
30  
31  
32  
33  
34  
35  
36  
37  
38  
39  
40  
41  
42  
43  
44  
45  
46  
47  
48  
49  
50  
51  
52  
53  
54  
55  
56  
57  
58  
59  
60

energy dispersive spectroscopy (XEDS) detector (Kevex detector with an ultrathin window).  
For the cryo-TEM measurements, samples were vitrified using a Leica EM GP immersion under controlled humidity and temperature<sup>48</sup>. Samples were deposited on glow-discharged electron microscope grids followed by blotting and vitrification by rapid freezing in liquid ethane (-184°C). Grids were transferred to a single-axis cryo-holder (model 626, Gatan) and were observed using a 200 kV electron microscope (Tecnai G2 T20 Sphera, FEI) equipped with a 4k × 4k CCD camera (model USC 4000, Gatan). Micrographs were acquired under low electron doses using the camera in binning mode 1 and at a nominal magnification of 50,000x. For the cryo-TXM measurements, samples were frozen using a Leica EM GP immersion freezer. The environmental chamber was kept at 20°C with 80% humidity. Four µL of the sample were dropped on a hydrophilized (air plasma treated using Henniker HPT-100 plasma treatment) carbon coated copper grid (Quantifoil R2/2 type grid). The grid was blotted with n°1 Whatman filter paper prior to freezing and then automatically plunged into liquid ethane. The samples were stored in liquid nitrogen until further use. The cryo-TXM images were recorded at the full field transmission soft X-ray microscope installed at the MISTRAL beamline<sup>49</sup> of the ALBA synchrotron. A capillary condenser lens after the monochromator exit slit focuses the radiation to the sample. After the sample, a Fresnel zone plate with outermost zone width of 25 nm was used as objective lens to record a magnified image on a direct illumination CCD detector (Pixis XO by Princeton Instruments with 1024 × 1024 pixels and 13 µm pixel size). The spatial resolution of the system is limited by the objective lens and was estimated to be 23 nm half pitch at 520 eV using a Siemens star pattern with 30 nm smallest features<sup>50</sup>. The magnification used for the transmission image was × 1300, corresponding to an effective pixel size of 10 nm. Twenty images with an exposure time of 3 seconds each were acquired and then averaged. The average transmitted intensity I and the corresponding Flat Field I0 (i.e. the incident intensity on the sample) were used to obtain the transmission T, related to the linear absorption coefficient

View Article Online  
DOI: 10.1039/D0EN00412J

Environmental Science: Nano Accepted Manuscript

of the sample by the Beer-Lambert law. The energy was set to 520 eV to maximize the contrast between water and carbon, calcium and iron rich regions of the imaged suspension.

## Results and discussion

### 1. *Iron speciation within aggregates*

Fe speciation within the aggregates was studied by XAS at Fe K-edge. The XANES spectra (Figure SI 2) are similar and representative of Fe(III) in an octahedral symmetry<sup>51</sup>. All EXAFS spectra exhibit a maximum of amplitude at 6.3 Å<sup>-1</sup> (Figure 1). Fe(II) and Fe(III)-oligomer spectra exhibit a damping shape that is close to monotonous. The oscillations of the Fe(II) spectra are shifted to low photoelectron wavevector,  $k$ , values as compared to Fe(III) species. Iron(III)-Np and Fh exhibit a shoulder at 5.1 Å<sup>-1</sup> and an oscillation at 7.5 Å<sup>-1</sup> that are more intense for Fh than Fe(III)-Np (Figure 1a). The Lp spectrum is well-structured with a shoulder at 4.7 Å<sup>-1</sup>, a strong oscillation at 7.2 Å<sup>-1</sup> and a smaller one at 7.9 Å<sup>-1</sup>. For the Fe-OM-Ca aggregates, the oscillations occurred at the same  $k$  values as the Fe(III) references evidencing the presence of Fe(III). More precisely, two different behaviours can be observed depending on the Fe/OC ratio. Spectra for Fe/OC = 0.02 exhibit a monotonous shape except at 7.5 Å<sup>-1</sup> where a shoulder occurs (Figure 1b). Samples formed at Fe/OC = 0.05 and Fe/OC = 0.08 exhibit more structured EXAFS spectra with an additional shoulder at 5.1 Å<sup>-1</sup> and a pronounced shoulder at 7.4 Å<sup>-1</sup> (Figure 1c and d).

Guénet *et al.*<sup>2</sup> demonstrated that nano-Lp coexist with small Fe-clusters bound to OM in riparian wetland soils. Similar results were demonstrated by ThomasArrigo *et al.*<sup>6</sup> who provided evidence of Fh and Lp occurrence in OM-rich environmental systems. Moreover, Vantelon *et al.*<sup>14</sup> demonstrated that within Fe(III)-OM aggregates for Fe/OC = 0.08, Fe(III)-oligomers and Fe(III)-Np occurred together. Linear combination fittings were performed on the EXAFS spectra of the Fe-OM-Ca aggregates using the signal of Fe(II), Fe(III)-oligomers, Fe(III)-Np, Fh and Lp. Only Fe(III)-oligomers and Fe(III)-Np EXAFS signals were necessary to reproduce



by LCF the experimental data for Fe/OC = 0.02 whereas for the highest Fe/OC ratio, Fe(III)-oligomers, Fe(III)-Np and Fh EXAFS signals were needed. If they exist, Fe(II) and Lp amount were below the detection limit (Figure 1 and Table SI 1). Several studies similarly demonstrated that with fulvic or humic acids, Fe(II) oxidation-hydrolysis did not produce Lp<sup>14,17,52</sup>. This discrepancy regarding the occurrence of Lp could be explained by the variability in the physico-chemical conditions prevailing during aggregate formation.

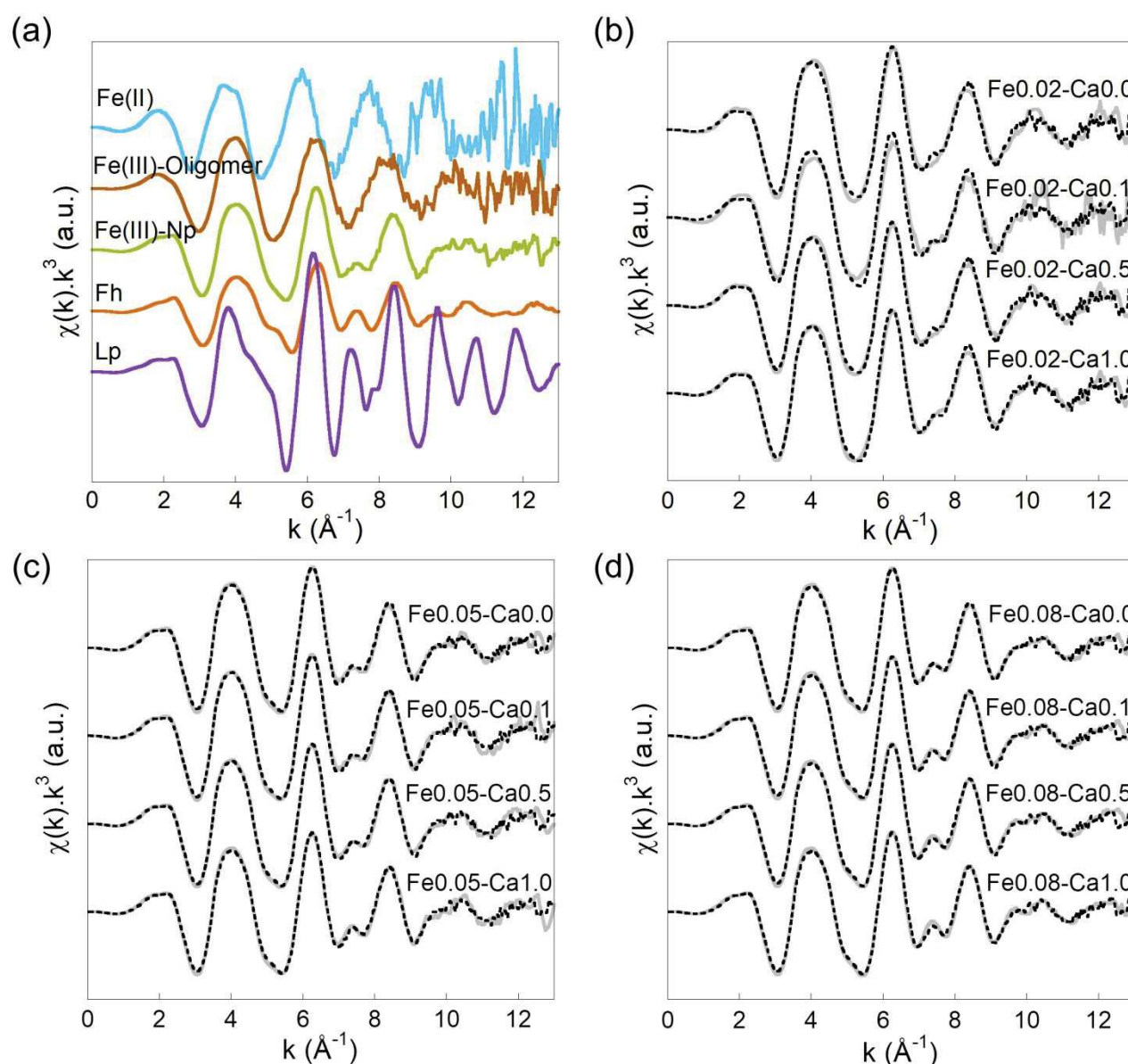


Figure 1 – Iron K-edge EXAFS spectra of (a) references used for LCF and samples at (b) Fe/OC = 0.02, (c) Fe/OC = 0.05 and (d) Fe/OC = 0.08. Solid lines are experimental data and dotted lines are the LCF results.

For Fe/OC = 0.02, and Ca/Fe = 0.0 and 0.1, the EXAFS signal features at 5.1 and 7.4 Å<sup>-1</sup> are

not perfectly reproduced by LCF. For  $\text{Fe/OC} = 0.08$ , Fe(III)-oligomers are described as tetramers bound to OM<sup>14</sup>. However, Vilg -Ritter *et al.*<sup>53</sup> and Mikutta *et al.*<sup>11</sup> described Fe(III)-oligomers as trimers for  $\text{Fe/OC} = 0.02$  and 0.004 respectively. For  $\text{Fe/OC} = 0.02$ , Fe(III) monomers bound to OM were also reported by Karlsson and Persson<sup>19</sup>. The tiny discrepancy observed between the data and LCF can therefore be explained by the difference in the  $\text{Fe/OC}$  ratio for the references used for fitting. The Fe(III)-Np signal may also be slightly different than the one used for the fit due to a particle size effect. In any case, for  $\text{Fe/OC} = 0.02$ , Fe occurs at around 30% as Fe(III)-oligomers and 70% as Fe(III)-Np irrespective of the Ca/Fe ratio (Figure 2). For  $\text{Fe/OC} = 0.05$  and 0.08, Fe is organized as Fe(III)-oligomers, Fe(III)-Np and Fh. With increasing  $\text{Fe/OC}$  and Ca/Fe, Fe(III)-Np remains constant (around 55%) whereas Fe(III)-oligomers amount decrease in favour of Fh until reaching a steady state at 13% Fe(III)-oligomers, 34% Fh and 53% Fe(III)-Np for  $\text{Fe/OC} = 0.08$  and  $\text{Ca/Fe} \geq 0.1$ . These results are in agreement with Chen *et al.*<sup>18</sup>. By co-precipitating Fe(III) with OM at  $\text{Fe/OC} = 0.44$ , they provided evidence that 72 % of Fe was organized as Fh and 28% as so-called “insoluble Fe(III)-OM” species (described by van Schaik *et al.*<sup>25</sup> as Fe trimers bound to OM).

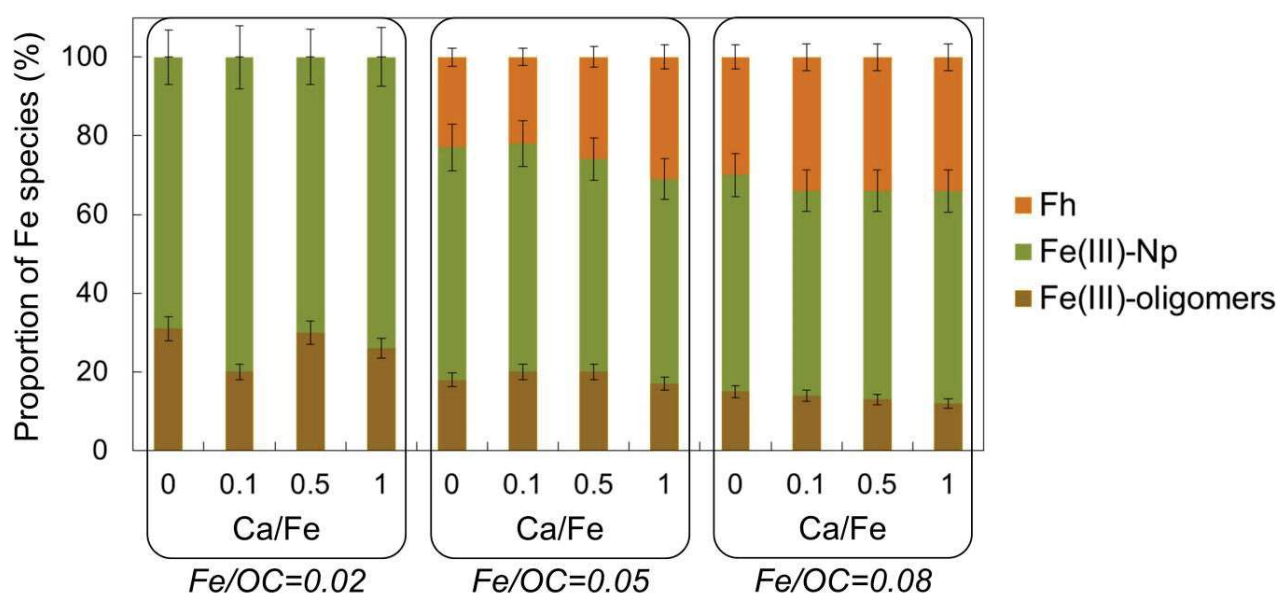


Figure 2 – Proportion of Fe(III)-oligomers (brown), Fe(III)-Np (green) and Fh (orange) determined by LCF of the EXAFS data shown in Figure 1.



2. Structural organization of Fe particles in the aggregates

View Article Online  
DOI: 10.1039/D0EN00412J

SAXS measurements are used to investigate the Fe part of Fe-OM-Ca aggregates (Figure 3). The X-ray contrast only depends on the electronic density of the element, which is significantly larger for Fe as compared to OM (the OM part is thus invisible in the scattering signal). The high q part of the scattering curve corresponds to the form factor of Fe primary beads (Fe-PB) that can be modelled with a spherical form factor with a radius equal to 0.8 nm. These Fe-PB are consistent with the coherent scattering domains of Fh described by Michel *et al.*<sup>54</sup>. All curves exhibit a shoulder between  $10^{-2}$  and  $10^{-1} \text{ \AA}^{-1}$  indicating a characteristic size of Fe, corresponding to Fe primary aggregates (Fe-PA) made of Fe-PB. This shoulder shifts to the lowest q with the increasing Ca/Fe ratio, indicating that the size of the Fe-PA increases. Two different behaviours of the inflexion shape can be observed depending on the Fe/OC ratio. For Fe/OC = 0.02, the inflexion is lower without Ca than with Ca. By contrast, the increasing Ca/Fe ratio leads to the attenuation of the inflexion for Fe/OC = 0.05 and 0.08. At low q, the increase in intensity indicates the aggregation of Fe-PA as larger objects, i.e. Fe secondary aggregates (Fe-SA) for which the size cannot be determined given the limited q range.

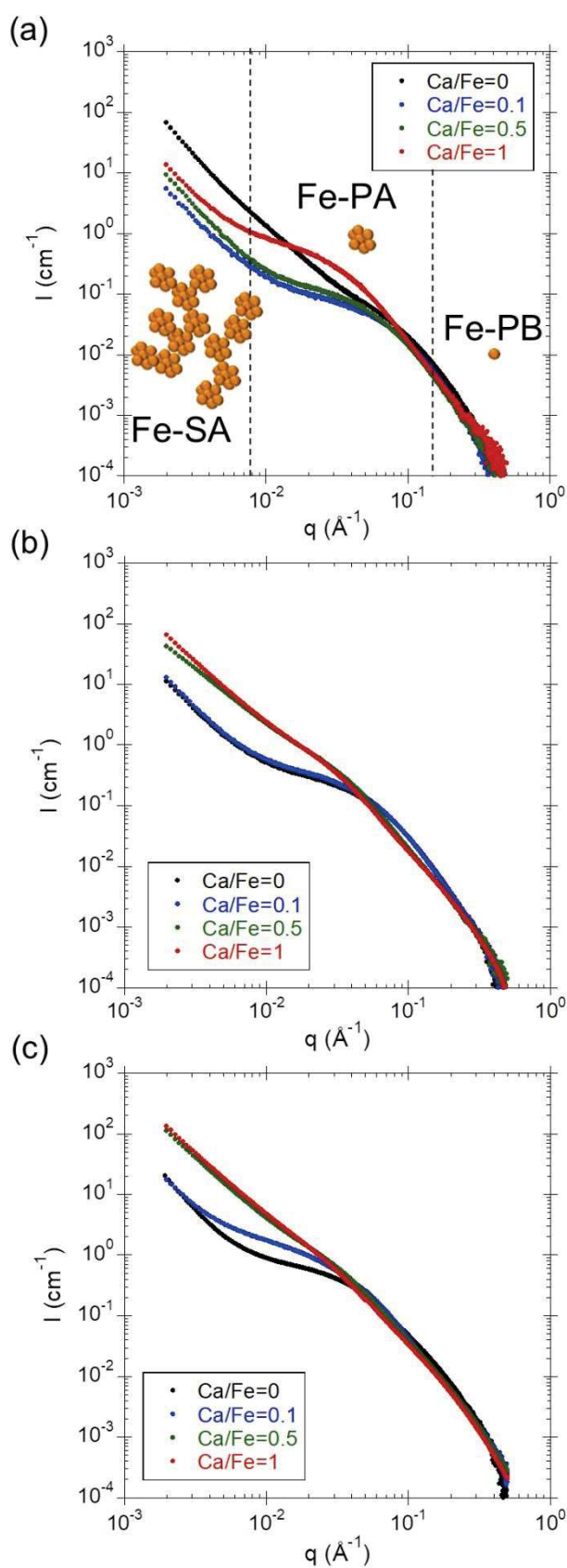


Figure 3 – SAXS curves for samples with (a)  $\text{Fe/OC} = 0.02$ , (b)  $\text{Fe/OC} = 0.05$  and (c)  $\text{Fe/OC} = 0.08$ . In (a) Fe-PB, Fe-PA and Fe-SA are represented in their corresponding scattering domain.

At intermediate  $q$ , the form factor of Fe-PA was extracted to determine their radius (Figure SI 4, Table SI 2 and Figure 4) which increases with the increasing Fe/OC ratio as demonstrated by Guénet *et al.*<sup>13</sup>. Furthermore, the Fe-PA size also increases with the increasing Ca/Fe ratio while their morphology remains constant as highlighted by the Fe-PA fractal dimension which is  $\approx 2.4$  irrespective of the Fe/OC or Ca/Fe ratio (Table SI 2).

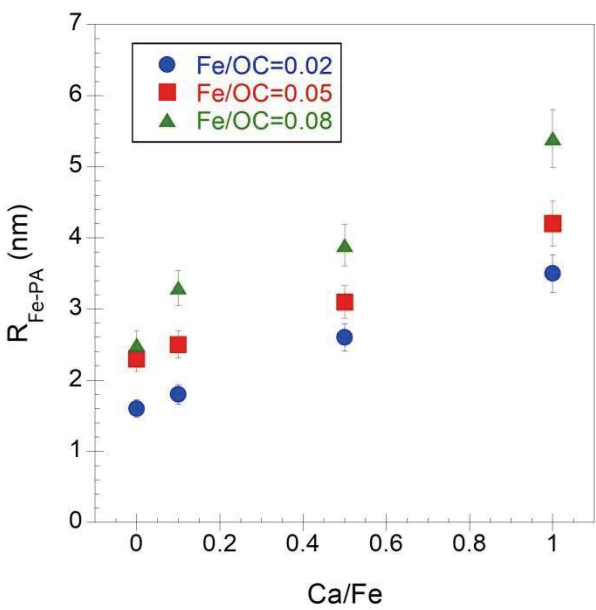


Figure 4 – Variations in the radius of the Fe primary aggregates relative to Ca/Fe for Fe/OC = 0.02 (blue circles), 0.05 (red squares) and 0.08 (green triangles).

The total structure factor ( $S_T(q)$ ) can be extracted by dividing the total scattering intensity by the form factor of Fe-PA (Figure SI 5). The increase of the  $S_T(q)$  intensity as a power law in the range  $8 \times 10^{-2}$ - $1 \times 10^{-3} \text{ \AA}^{-1}$  is relevant to the Fe-SA contribution. The shoulder observed between  $3 \times 10^{-1}$  and  $7 \times 10^{-2} \text{ \AA}^{-1}$  in  $S_T(q)$  indicates interactions between the Fe-PA inside the Fe-SA. This shoulder can be used to calculate the centre-to-centre distance  $d_0$  between Fe-PA within Fe-SA (Table 2 and Figure SI 5). For samples exhibiting the lowest Ca contents,  $d_0$  increases with increasing Fe/OC and Ca/Fe ratios as a response to the increase in Fe-PA size since the  $d_0$  values range from  $2 \times R_{PA}$  to  $2.8 \times R_{PA}$ . However, the key result is observed for the four samples exhibiting the highest Ca contents for which no peak occurred, suggesting a loss of correlation between Fe-PA in response to a longer distance between Fe-PA and/or a larger  $d_0$  dispersity.

As a result, the presence of Ca leads to a long range correlation between the Fe-primary aggregates.

Table 2 – Values of the centre-to-centre distance  $d_0$  between Fe-PA. A ‘-’ is reported when the correlation peak of Fe-PA did not occur, indicating an increase in the distance between Fe-PA.

$d_0$ (nm)		Ca/Fe			
		0.0	0.1	0.5	1.0
Fe/OC	0.02	4.4	4.9	6.0	6.5
	0.05	5.5	5.9	-	-
	0.08	4.7	7.2	-	-

At Fe/OC = 0.05, TEM observations showed black spherical entities (Figure 5). The XEDS analysis revealed the presence of Fe indicating that these black dots are Fe particles, as previously observed for synthetic and natural samples<sup>3,13,55</sup>. Their compact spherical and nanometric size (between 2 and 6 nm) is consistent with Fe-PA identified by SAXS. Moreover, their size increases with the increasing Ca/Fe ratio from  $\approx$  2 nm for Fe0.05-Ca0.0 and Fe0.05-Ca0.1 (Figure 5a and b) to  $\approx$  5.5 nm for Fe0.05-Ca1.0 (Figure 5d), confirming the SAXS results.



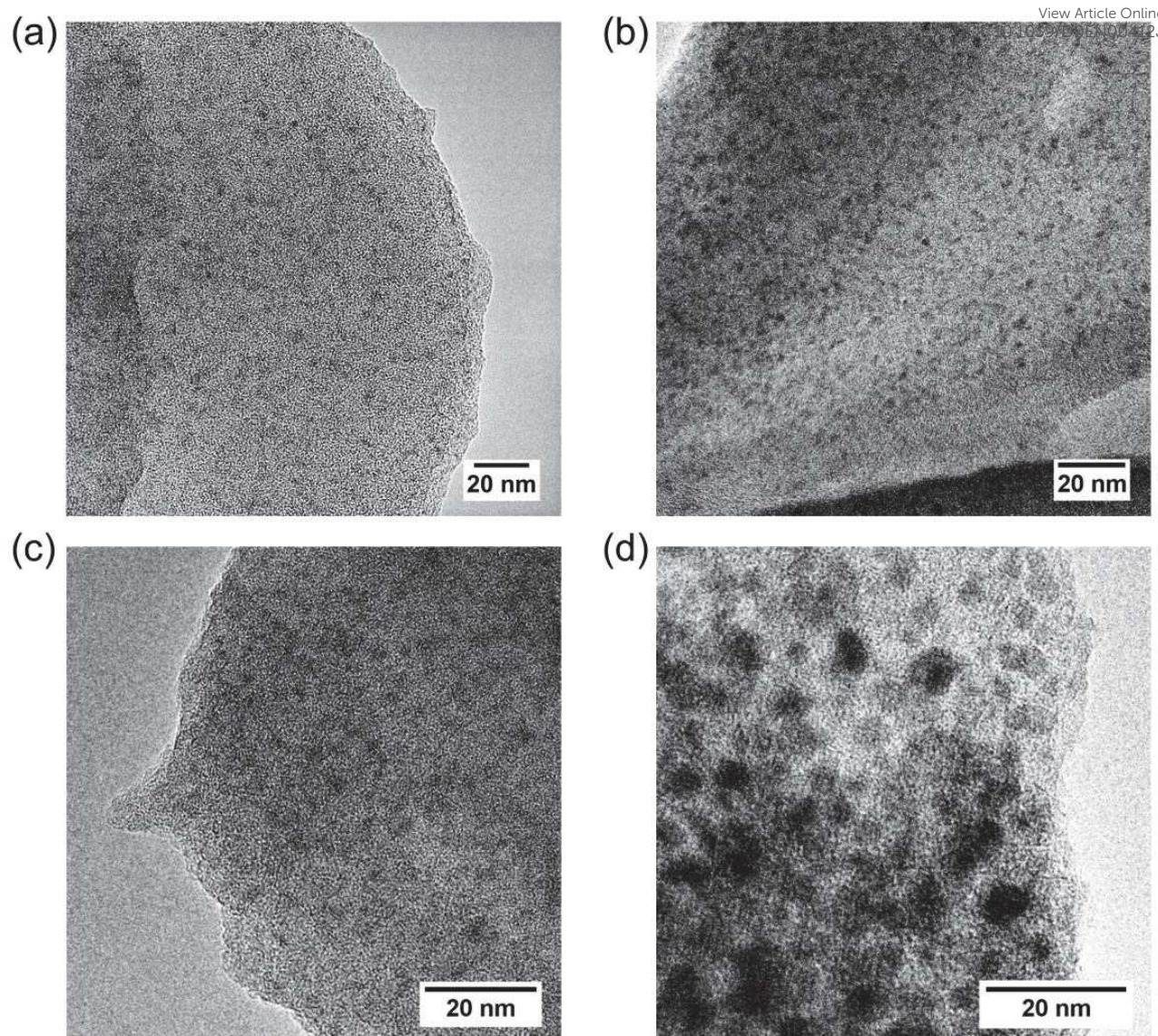


Figure 5 – Transmission electron microscopy images of the aggregates for Fe/OC = 0.05 and (a) Ca/Fe 0, (b) Ca/Fe 0.1, (c) Ca/Fe 0.5 and (d) Ca/Fe 1. The grey scales are arbitrary.

### 3. *Structural arrangement of OM in the aggregates*

SANS measurements with a 100 % D<sub>2</sub>O contrast allowed to match the iron scattering contribution to the signal and to access the OM part of the aggregates. For SANS curves with 100 % D<sub>2</sub>O contrast (Figure 6a,b,c), the inflexion observed for  $q < 10^{-3} \text{ \AA}^{-1}$  suggests a typical size for the OM aggregates. This inflexion shifts to the lower  $q$  when increasing Ca/Fe ratio suggesting an increase of the OM size. However, these curves exhibit the same slope in the  $q$  domain between  $10^{-3}$  and  $10^{-1} \text{ \AA}^{-1}$  irrespective to the Fe/OC or the Ca/Fe ratio, suggesting no local scattering contribution from OM phases. To enforce this observation, SANS curves with

50/50% H<sub>2</sub>O/D<sub>2</sub>O contrast were measured (Figure 6d,e,f). At this specific contrast, both the contribution of OM and the Fe is visible. For  $q > 10^{-2} \text{ \AA}^{-1}$ , this contrast can also be used to test if another OM organization (e.g. smaller molecules than the OM aggregates) could contribute to the signal. In the  $q$  domain between  $10^{-3}$  and  $10^{-2} \text{ \AA}^{-1}$ , no differences were observed between samples as all the curves exhibit the same slope. In the  $q$  domain between  $10^{-2}$  and  $10^{-1} \text{ \AA}^{-1}$ , an inflexion occurs for samples with the highest Ca/Fe ratios, suggesting a variation in the local organization. In this range, the SANS and SAXS curves can be superimposed showing an identical signal provided mainly by Fe-PA (Figure SI 6). This result confirms that no local modification of OM occurs as its local scattering contribution is the same irrespective of the Fe/OC and Ca/Fe ratios.

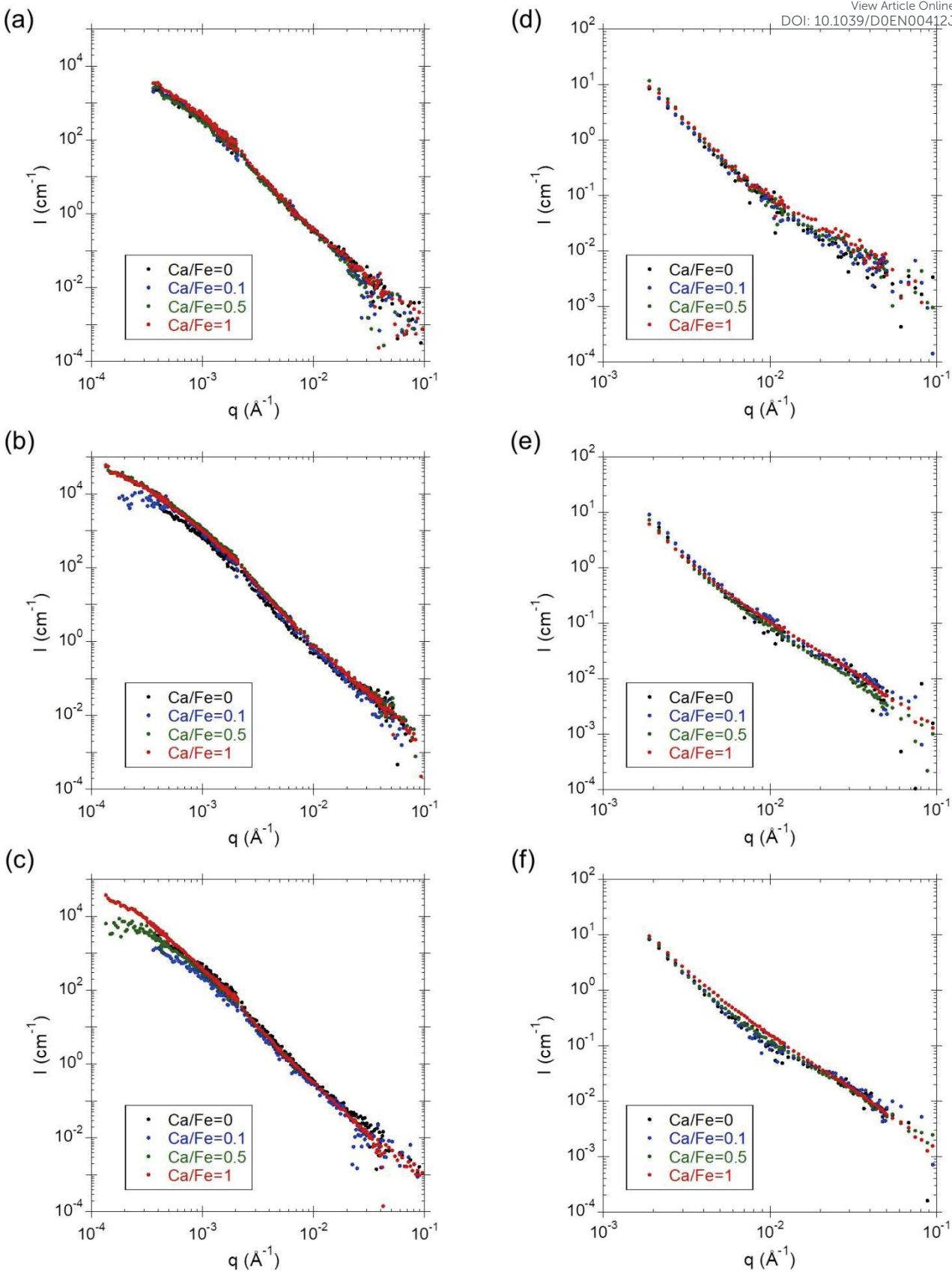


Figure 6 – SANS curves with 100% D<sub>2</sub>O contrast for samples with a Fe/OC ratio of (a) 0.02, (b) 0.05 and (c) 0.08, and with contrast at 50/50% H<sub>2</sub>O/D<sub>2</sub>O for samples with a Fe/OC ratio of (d) 0.02, (e) 0.05 and (f) 0.08.



All 100% D<sub>2</sub>O contrast curves were fitted with the Guinier-Porod equation (eq. 2) (Figure SI 7). The parameters used are reported in Table SI 3. All curves exhibit a fractal dimension,  $D_f$  around 2.8, consistent with previous observations on synthetic samples<sup>13</sup> and natural samples<sup>56,57</sup>. However, several studies reported a  $D_f$  value for OM between 2 and 2.5<sup>58–60</sup>. Osterberg and Mortensen<sup>59</sup> and Guénet *et al.*<sup>13</sup>, applied a Guinier model on natural and synthetic aggregates at Fe/OC = 0 or 0.01, respectively to obtain a gyration radius for OM from 30 nm<sup>59</sup> to approximately 100 nm<sup>13</sup>. The Guinier plateau tends to disappear with the increasing Fe/OC ratio in Guénet *et al.*<sup>13</sup> and Osterberg and Mortensen<sup>59</sup>. However, Diallo *et al.*<sup>58</sup> did not observe the same trend for natural aggregates. In our work, VSANS was used to reach lower  $q$ , to provide better evidence of a Guinier plateau and to calculate the typical OM size (Figure 7 and Table SI 3). The results showed an increase in OM size with the increasing Ca/Fe ratios without any local reorganization of the OM phase.

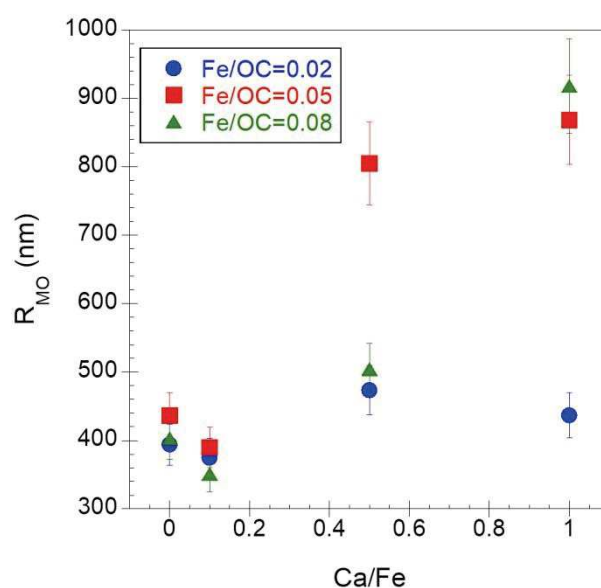


Figure 7 – Evolution of the OM radius relative to Ca/Fe ratio.

#### 4. Calcium interaction with the aggregates

Calcium interactions with the components of the Fe-OM aggregates were characterized by collecting XAS spectra at Ca K-edge. XANES spectra exhibit a pre-edge at 4041 eV which is assigned to the 1s→3d transition<sup>61,62</sup> with electric dipole character when the 3d orbitals are



hybridized with p orbitals and electric-quadrupole one (Figure 8). The  $1s \rightarrow 3d$  electric dipole transition is forbidden for centrosymmetric complexes, then pre-edge structure gains only weak intensity from electric quadrupole transition. In calcite, Ca is surrounded by six O in an octahedral geometry<sup>63</sup> so that the intensity of its pre-edge is relatively weak. The white line at 4045 eV represents the  $1s \rightarrow 4p$  transition and the resonance at 4072 eV corresponds to a  $KL_{II,III}$  multielectronic excitation<sup>62</sup>. Thus, according to Martin-Diaconescu *et al.*<sup>61</sup>, in our samples the lack of structure in the XANES spectra and the high intensity of the pre-edge indicate that more than six O are surrounding Ca in the first coordination shell.

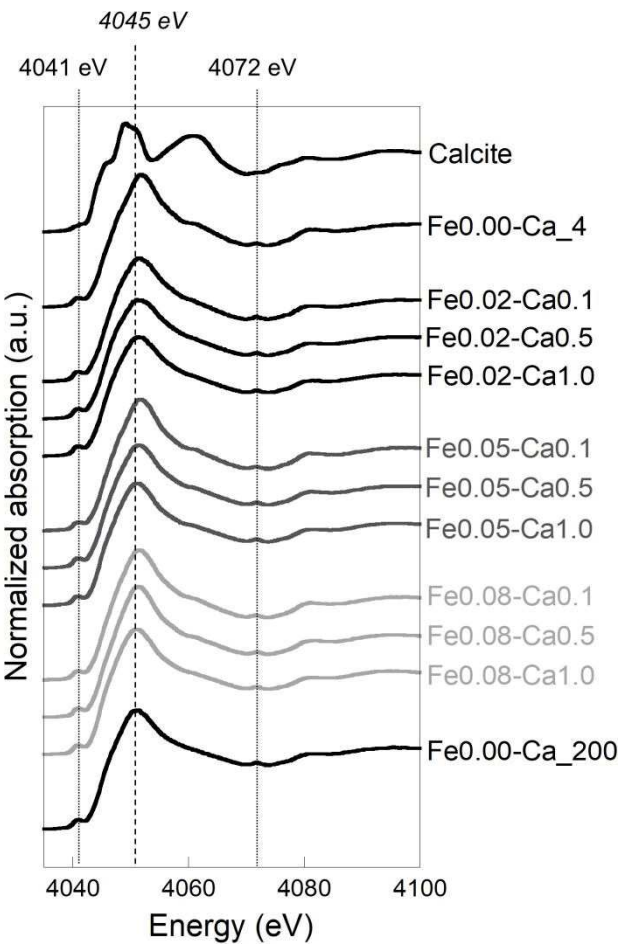


Figure 8 – Ca K-edge XANES spectra for sample.

Magnitude of EXAFS Fourier transform exhibits a first intense peak at 1.8 Å corresponding to the contribution of oxygens neighbours in the first coordination shell (Figure 9). A shoulder is visible for the highest Ca content at 2.1 Å. A second weak oscillation is observable at 2.8 Å and

a third more intense peak occurs at 3.3 Å, not corrected from phase shift. EXAFS spectra (Figure SI 8) exhibit a maximum of amplitude at 4.5 Å<sup>-1</sup>. A signal shift can be observed at the low k value for the highest Ca concentration. Two weak shoulders are also observed at 4 and 6 Å<sup>-1</sup>. Spectra were first fitted using two Ca-O distances (Ca-O1 at 2.31 Å and Ca-O2 at 2.48 Å) for the first coordination shell of Ca that was used to reconstruct the first Fourier transform peak. The second peak was fitted with two different C as second neighbours (Ca-C1 at 3.10 Å and Ca-C2 at 3.60 Å). A contribution of Ca as third nearest neighbours at 3.85 Å was then used to fit the third peak, providing evidence of the formation of Ca dimers. The complete fit results are reported in Table 3. The detailed shell-by-shell fitting is reported in Figure SI 9.

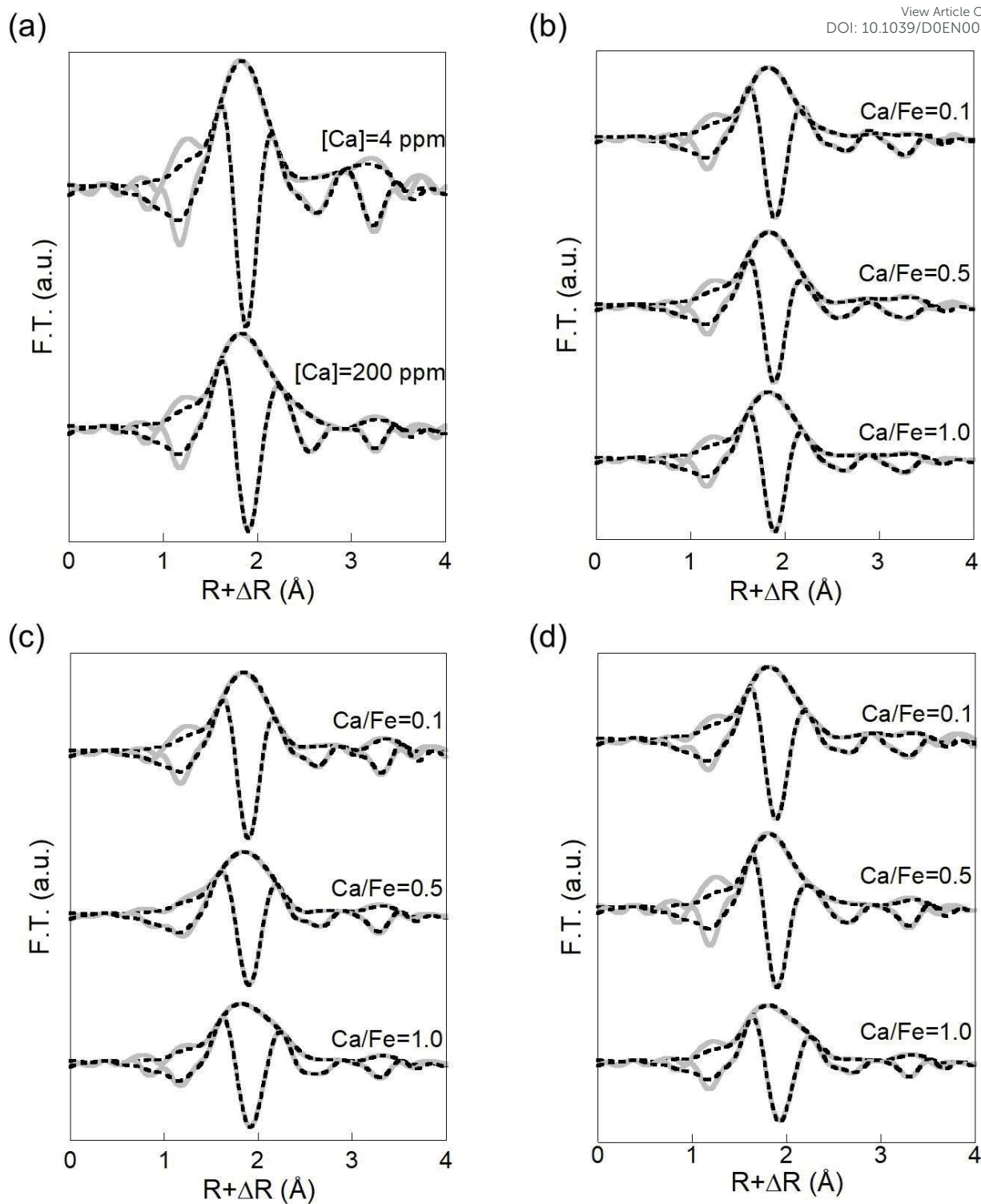


Figure 9 – Magnitude and imaginary part of the Fourier transform of the Ca K-edge EXAFS spectra for sample (a) without Fe, (b) Fe/OC = 0.02, (c) Fe/OC = 0.05 and (d) Fe/OC = 0.08. The grey solid lines are the experimental data and the black dotted lines are the fit results.

Table 3 – Ca K-edge EXAFS fit results.

Sample	R-factor	Ca-O1		Ca-O2		Ca-C1		Ca-C2		Ca-Ca	
		<i>N</i>	<i>R</i> (Å)	<i>N</i>	<i>R</i> (Å)	<i>N</i>	<i>R</i> (Å)	<i>N</i>	<i>R</i> (Å)	<i>N</i>	<i>R</i> (Å)
OM-[Ca]=4 ppm	0.0089	3.6	2.31	3.0	2.46	0.4	3.10	3.7	3.61	1.1	3.82
Fe0.02-Ca0.1	0.0033	3.4	2.31	3.2	2.47	0.5	3.09	2.7	3.59	0.9	3.83
Fe0.02-Ca0.5	0.0028	3.4	2.31	2.7	2.48	0.6	3.07	2.2	3.59	0.6	3.84
Fe0.02-Ca1.0	0.0029	3.1	2.31	2.8	2.47	0.6	3.09	2.0	3.58	0.6	3.82
Fe0.05-Ca0.1	0.0037	3.6	2.32	3.1	2.47	0.7	3.08	2.4	3.57	1.1	3.85
Fe0.05-Ca0.5	0.0035	2.9	2.30	3.3	2.46	0.6	3.09	2.0	3.61	0.8	3.84
Fe0.05-Ca1.0	0.0012	3.1	2.32	3.6	2.49	1.1	3.08	1.8	3.62	0.7	3.85
Fe0.08-Ca0.1	0.0024	3.6	2.31	3.3	2.48	0.6	3.10	2.6	3.60	0.8	3.85
Fe0.08-Ca0.5	0.0100	3.8	2.33	3.1	2.51	1.0	3.12	1.9	3.63	0.8	3.85
Fe0.08-Ca1.0	0.0038	3.0	2.33	3.2	2.51	0.7	3.14	1.3	3.66	0.6	3.86
OM-[Ca]=200 ppm	0.0026	3.0	2.32	3.0	2.49	1.4	3.07	1.3	3.60	0.5	3.81

The amplitude reduction factor  $S_0^2$  and the energy shift parameter  $\Delta E$  were respectively set to 1.00 and 4.95 eV by fitting the signal of calcite over the range of 1.3-4 Å (the calcite fit is reported in Figure SI 10 and the corresponding fitting parameters are reported in Table SI 4). *N* is the coordination number and *R* is the interatomic distance (Å). The Debye-Waller factors  $\sigma^2$  were fixed to 0.004 Å<sup>2</sup> to compare the evolution of each coordination number. The error on *N* and *R* are usually estimated to be  $\pm 10\%$  and  $\pm 1\%$ , respectively.

1  
2  
3  
4  
5  
6  
7  
8  
9  
10  
11  
12  
13  
14  
15  
16  
17  
18  
19  
20  
21  
22  
23  
24  
25  
26  
27  
28  
29  
30  
31  
32  
33  
34  
35  
36  
37  
38  
39  
40  
41  
42  
43  
44  
45  
46  
47  
48  
49  
50  
51  
52  
53  
54  
55  
56  
57  
58  
59  
60

The O number in the first coordination shell remains constant at  $6.5 \pm 0.6$  for all the samples. This result is consistent with XANES data and is representative of a Ca coordination number higher than six for an organic Ca complex<sup>61</sup> or hydrated soluble Ca<sup>62</sup>. In the second coordination shell, the C number also remains constant around  $2.8 \pm 0.3$ . Carbon in the second coordination shell is characteristic of the formation of Ca-OM inner sphere complexes. The Ca number was also constant around  $0.8 \pm 0.1$  demonstrating the formation of dimers. The Ca-Ca distance at 3.85 Å corresponds to Ca dimers bound by two O. To summarize, Ca forms dimers bound to OM as an inner sphere complex. Performing OC sorption experiments on Fh with Ca, Sowers *et al.*<sup>64</sup> suggested the formation of Fe-Ca-OC ternary complexes in which Fe was bound to Ca via an O. The presence of the Ca-OC inner complex occurrence is consistent with Ca binding to OM via carboxylic group as previously observed by Kalinichev and Kirkpatrick<sup>31</sup> and Iskrenova-Tchoukova *et al.*<sup>65</sup>. In their studies, binding with phenolic groups was also suggested. However, for our experimental pH at 6.5, phenolic groups remain protonated and weakly available for binding<sup>32</sup>. Moreover, during reduction, Adhikari *et al.*<sup>35</sup> reported a higher release and degradation of phenolic OC as compared to carboxylic OC. Here, Ca binding to carboxylic groups is therefore the more expected process and no Fe neighbour could be added in the fit of the second coordination shell of the Ca EXAFS.

5. Overall organization of Fe-OM-Ca aggregates

The overall organization of Fe-OM-Ca associations was observed by cryo-TEM (Figure 10a,b and c) and cryo-TXM imaging (Figure 10d). The cryo-TEM observation of Fe0.08-Ca0.1 (Figure 10a) exhibits dispersed black spherical entities consistent with Fe-PA described from SAXS and observed by TEM (Figure 5). The yellow arrows highlight dots showing higher Fe-PA density locally. They are embedded in a less intense background of  $\sim 100$  nm which could be assigned to an OM aggregates. This aggregate was subjected to electron beam irradiation. During irradiation, some bubbles were formed (red arrows on Figure 10b) which indicates

damaged organic compounds. Consequently, the  $\sim 100$  nm aggregate highlighted by yellow arrows was assigned to Fe-SA in an OM aggregate as described by Guénet *et al.*<sup>13</sup>. By contrast, for higher concentrations of Ca, cryo-TEM observation of Fe<sub>0.08</sub>-Ca<sub>0.5</sub> displays dispersed black dots embedded in a dark background (Figure 10c). These observations indicate Fe-PA embedded in an OM matrix and therefore correspond to an OM network trapping Fe-PA. The cryo-TXM observation of the same sample (Figure 10d) revealed darker features at the centre and on the right of the image, indicating the presence of OM, Ca and Fe that confirms the micrometric network formation. These results clearly provide evidence for the significant impact of Ca on Fe-OM structural organization, varying from aggregates to a micrometric network.



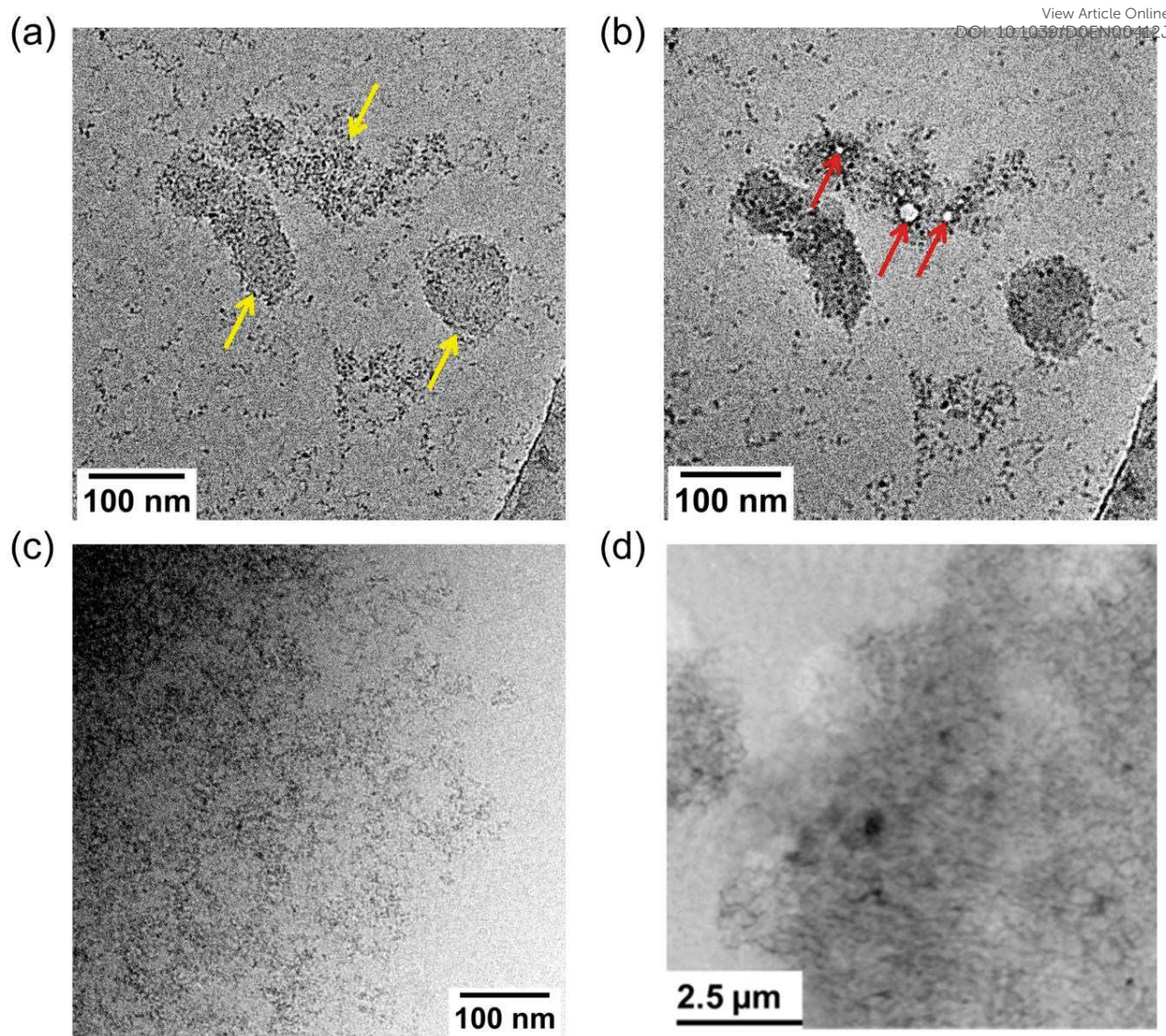


Figure 10 – Cryo-TEM imaging of (a) Fe<sub>0.08</sub>-Ca<sub>0.1</sub>, (b) Fe<sub>0.08</sub>-Ca<sub>0.1</sub> after electron beam irradiation, (c) Fe<sub>0.08</sub>-Ca<sub>0.5</sub> and (d) cryo-TXM imaging of Fe<sub>0.08</sub>-Ca<sub>0.5</sub>. The dense part at the bottom right in (a) and (b) corresponds to the thin carbon film on the grid. The 2 μm white circles and a grey background in the top left of (d) correspond to the holes and the carbon film on of the grid, respectively.

The formation of a micrometric network was also confirmed with filtration and ultrafiltration experiments (Table 4). For Fe<sub>0.08</sub>-Ca<sub>0.1</sub> the presence of OM, Fe and Ca in the > 0.2 μm and 0.2 μm-30 kDa fractions demonstrated the existence of aggregates with a size < 200 nm. For Fe<sub>0.08</sub>-Ca<sub>0.5</sub>, 96 % of the OC and 100 % of the Fe is in the > 0.2μm fraction while SAXS measurements and TEM observations provided evidence of the existence of Fe-PA with a size ≈ 5 nm. These results encouraged the formation of an OM micrometric network trapping Fe-PA.

Table 4 – OC, Ca and Fe concentration (mmol L<sup>-1</sup>) for Fe0.08-Ca0.1 and Fe0.08-Ca0.5. <LOD: below the limit of detection (LOD).

Fractions	Fe0.08-Ca0.1			Fe0.08-Ca0.5		
	OC	Ca	Fe	OC	Ca	Fe
>0.2 $\mu$ m	36.5 $\pm$ 3.2	0.35 $\pm$ 0.02	3.4 $\pm$ 0.3	54.9 $\pm$ 2.1	1.2 $\pm$ 0.1	4.77 $\pm$ 0.1
0.2 $\mu$ m-30 kDa	17.4 $\pm$ 3.2	0.17 $\pm$ 0.03	1.6 $\pm$ 0.3	<LOD	<LOD	<LOD
<30 kDa	2.3 $\pm$ 0.3	0.05 $\pm$ 0.01	<LOD	2.2 $\pm$ 0.4	1.2 $\pm$ 0.1	<LOD

### Fe-OM-Ca associations: from aggregates to a micrometric network

It was demonstrated that calcium controls the structural organization of the Fe-OM-Ca association through its binding to OM via carboxylic groups (COOH). It is thus appropriate to present the results depending on Ca/OC molar ratio since SANS measurements highlight a significant increase of the OM size from  $\text{Ca/OC} \geq 0.026$  (Figure 11). This observation is in accordance with cryo-TEM and cryo-TXM images which provide evidence of the OM micrometric network formation from  $\text{Ca/OC} \geq 0.026$ .

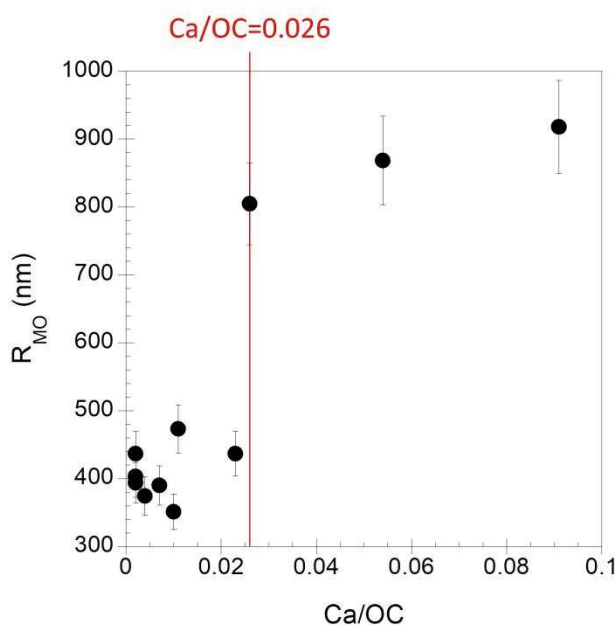


Figure 11 – Evolution of the OM radius relative to Ca/OC ratio.

Fe-OM-Ca associations therefore exhibit two distinct organizations depending on the Ca/OC ratio. For  $\text{Ca/OC} < 0.026$ , Fe-OM-Ca associations are organized as aggregates. Iron exhibits a fractal organization in which Fe-PB (radius  $\approx 0.8$  nm) formed Fe-PA (radius  $\approx 5$  nm) that is



1  
2  
3  
4  
5  
6  
7  
8  
9  
10  
11  
12  
13  
14  
15  
16  
17  
18  
19  
20  
21  
22  
23  
24  
25  
26  
27  
28  
29  
30  
31  
32  
33  
34  
35  
36  
37  
38  
39  
40  
41  
42  
43  
44  
45  
46  
47  
48  
49  
50  
51  
52  
53  
54  
55  
56  
57  
58  
59  
60

either isolated or embedded in an OM aggregate (radius  $\leq 100$  nm) resulting in the formation of Fe-SA (radius  $> 100$  nm), as already described<sup>13</sup> (Figure 12, left). For  $\text{Ca/OC} \geq 0.026$ , the organization of the Fe-OM-Ca association is drastically different. All OM is branched out by Ca and forms a micrometric network in which all Fe-PB and Fe-PA are embedded (Figure 12, right). The presence of Ca also results in an increase in Fe-PA size from 2 nm to 5 nm. Therefore, while Ca did not directly interact with Fe, Ca atoms screen interactions between Fe and OM thereby allowing for the growth of Fe-PA. Calcium drives the organizational mechanism of OM which in turn controls the size and the distribution of Fe-PA in the OM aggregate or in the OM network. Thus, calcium drives the structural transition in this system. These significant modifications of the structural organizations modify the size of the global aggregates and their colloidal stability (Figure SI 1). For  $\text{Ca/OC} < 0.026$ , Fe-OM-Ca associations are composed of aggregates which stay in suspension and can be transported with the water flow. For  $\text{Ca/OC} \geq 0.026$ , the formation of a micrometric network results in the settlement of Fe-OM-Ca associations and their immobilization by gravitational settling and/or trapping the soil porous media<sup>66</sup>.

View Article Online  
DOI: 10.1039/D0EN00412J

Environmental Science: Nano Accepted Manuscript

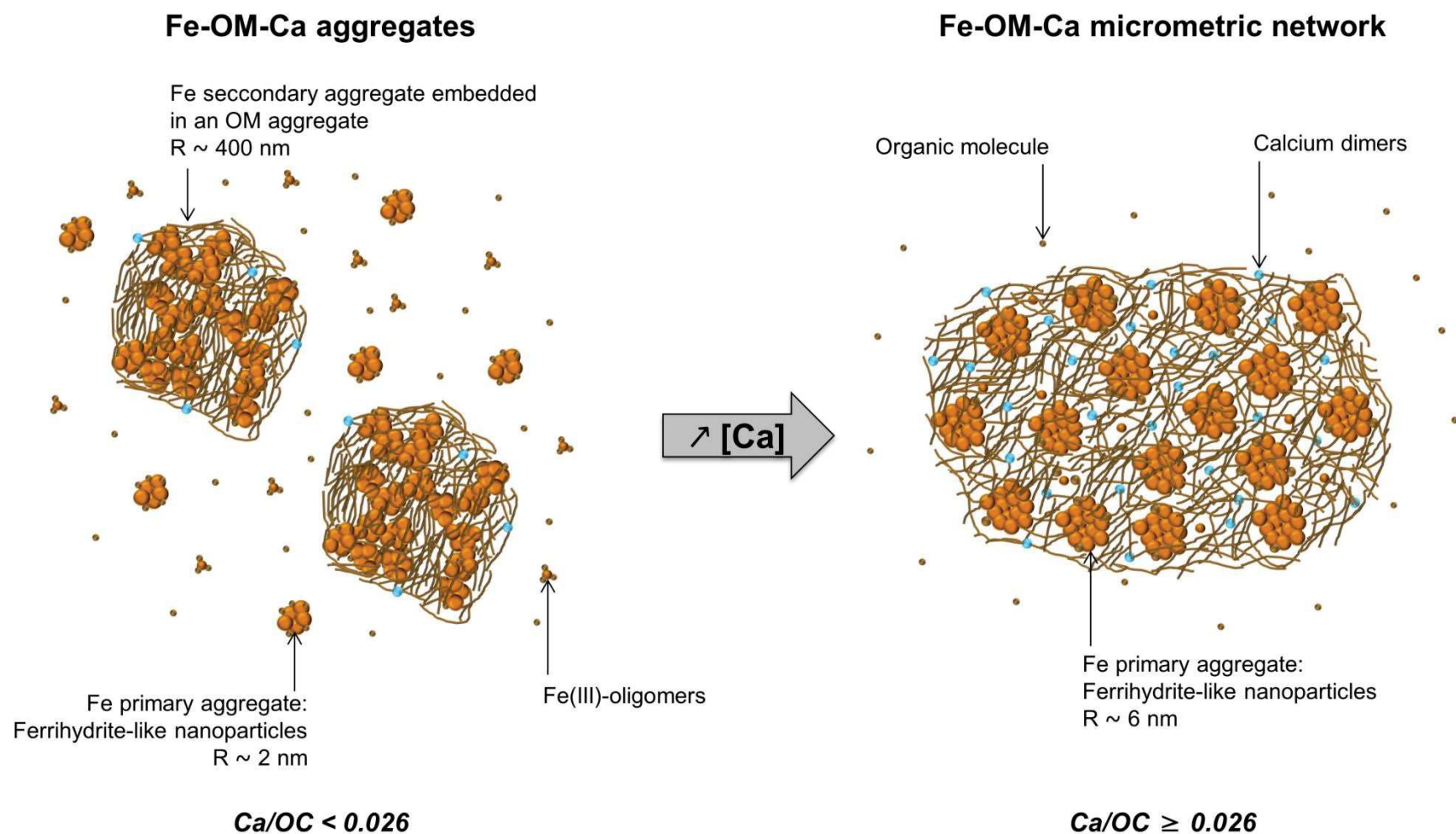


Figure 12 – Schematic representation of the structural organization of the Fe-OM-Ca associations depending on the Ca/OC ratio.

1  
2  
3  
4  
5  
6  
7  
8  
9  
10  
11  
12  
13  
14  
15  
16  
17  
18  
19  
20  
21  
22  
23  
24  
25  
26  
27  
28  
29  
30  
31  
32  
33  
34  
35  
36  
37  
38  
39  
40  
41  
42  
43  
44  
45  
46  
47  
48  
49  
50  
51  
52  
53  
54  
55  
56  
57  
58  
59  
60

In environmental waters, OM is known to control Fe phases by inhibiting their growth and crystallinity. Organic matter also enables the formation of complexes formed with a Fe oligomer and its carboxylic functional group<sup>13–15,17</sup>. Given that Leonardite HA is composed of  $7.46 \times 10^{-3}$  mol of COOH per gram of C<sup>67</sup>, an apparent COOH concentration can be calculated for our samples (Table 5). In Fe-OM-Ca associations, Ca is bound to OM via COOH with a COOH/Ca = 3. For Fe0.08-Ca0.1, the COOH/Ca ratio within aggregates is close to 9 and therefore some carboxylic groups remain available for the Fe phases. For Fe0.08-Ca0.5, COOH/Ca = 4.2 in the OM micrometric network. As a consequence, carboxylic groups are less available for binding the Fe species. In the OM network, Fe phases are not as covered by the organic molecule and their adsorption capacity should therefore be higher. Furthermore, for the highest Ca amounts, the Fe(III)-oligomer content decreases in favour of Fh, increasing the sorption capacities of the Fe aggregates. Conversely, the size of the nanoparticulate Fe phases is allowed to increase and nanoparticles larger than 20 nm exhibit lower adsorption capacities<sup>68</sup>. The Fe-OM-Ca adsorption capacities could therefore be lower with increasing Ca amounts and the subsequent continuous network formation. The formation of a continuous network leads to two antagonist effects with regard to the Fe-OM-Ca adsorption capacities, which need to be investigated in further studies. In addition, the presence of Ca should impact the Fe-OM aggregates reactivity regards bioreduction processes. Pédrot *et al.*<sup>17</sup> demonstrated that the bioreduction of Fe(III)-OM colloids was significantly faster than that of nano-Lp. They suggested that OM acts as an electron shuttle during the reduction process. Adhikari *et al.*<sup>35</sup> reported a decrease of the Fh-OM co-precipitates bioreduction rate in the presence of Ca. The partial screening of the interactions between Fe and OM evidenced in our study could explain this result: the OM, bound to Ca, could not act as electron shuttle anymore.

View Article Online  
DOI: 10.1039/D0EN00412J

Environmental Science: Nano Accepted Manuscript

Table 5 – Concentration of the carboxylic groups (COOH) (mol L<sup>-1</sup>) and COOH/Ca ratios for Fe0.08-Ca0.1 and Fe0.08-Ca0.5.

Fractions	Fe0.08-Ca0.1		Fe0.08-Ca0.5	
	COOH (mol L <sup>-1</sup> )	COOH/Ca	COOH (mol L <sup>-1</sup> )	COOH/Ca
> 0.2 μm	3.22×10 <sup>-3</sup>	9.2	4.92×10 <sup>-3</sup>	4.2
0.2 μm-30 kDa	1.56×10 <sup>-3</sup>	8.7	-	-

## Conclusion

We demonstrated the impact of Ca on the structural organization of Fe-OM aggregates. The structural organization of Fe-OM-Ca associations is controlled by the occurrence of Ca through its binding to OM carboxylic groups. Fe-OM-Ca associations can have two distinct organizations depending on the Ca/OC ratio. For low Ca concentrations, Fe-OM-Ca associations are organized as aggregates in which Fe exhibits three aggregation levels: (i) isolated Fe primary beads bound to organic molecules, that can be aggregated as (ii) Fe primary aggregates which can themselves form (iii) Fe secondary aggregates embedded in an OM aggregate (Figure 12). A structural transition occurs with the increasing Ca/OC ratio until an OM micrometric network is formed. This structural transition is driven by Ca which mainly interacts with OM COOH sites. Calcium acts as a bridge between the organic molecules and allows the formation of a large OM network. As organic molecules are preferentially connected to each other by Ca bridges, they are less available for binding Fe which is less covered by OM, allowing for the growth of ferrihydrite-like nanoparticulate structures as indicated by their size increase. The impact of Ca on the overall structural organization is of major importance regarding the increase of Ca amounts in surface waters due to the permafrost thawing, which one is enhanced by climate change<sup>69</sup>. Moreover, the interaction of Ca with OM increases the Fh-like binding sites availability and prevents the ability of OM to act as an electron shuttle in bioreduction processes. Finally, the Ca occurrence controls the mobility of Fe-OM aggregates and associated elements through the formation of a micrometric network.

**Acknowledgments**

This study is part of a Ph.D. funded by the French administrative region Brittany and by the SOLEIL-LLB through the ‘ORPHREA’ project and the French “Institut national des sciences de l’Univers” (INSU) through the “Initiative Structurante EC2CO – BIOHEFECT” allocated to Dr. Delphine Vantelon via the ‘ISAAP’ project. The authors are grateful to Dr. Gildas Ratié for his help in presenting the figures. Ludivine Rault is acknowledged for the TEM observations. The authors acknowledge SOLEIL for beamtime allocation at the LUCIA beamline (proposal 99170211) and ROCK beamline (proposal 20170795). The work at ROCK was supported by a public grant overseen by the French National Research Agency (ANR) as a part of the “Investissements d’Avenir” program ref: ANR-10-EQPX-45. These experiments were performed at MISTRAL beamline at ALBA Synchrotron with the collaboration of ALBA staff. This work is based upon experiments performed at the KWS-2 and KWS-3 instruments operated by JCNS at the Heinz Maier-Leibnitz Zentrum (MLZ), Garching, Germany. The authors gratefully acknowledge the financial support provided by JCNS to perform the neutron scattering measurements at the Heinz Maier-Leibnitz Zentrum (MLZ), Garching, Germany. This work benefited from the use of the SasView application, originally developed under NSF award DMR-0520547. SasView contains code developed with funding from the European Union’s Horizon 2020 research and innovation programme under the SINE2020 project, grant agreement No 654000. Dr Sara Mullin is acknowledged for post-editing the English style.

Environmental Science: Nano Accepted Manuscript

## References

View Article Online  
DOI: 10.1039/D0EN00412J

- 1 N. S. Wigginton, K. L. Haus and M. F. Hochella Jr, Aquatic environmental nanoparticles, *J. Environ. Monit.*, 2007, **9**, 1306.
- 2 H. Guénet, M. Davranche, D. Vantelon, M. Pédro, M. Al-Sid-Cheikh, A. Dia and J. Jestin, Evidence of organic matter control on As oxidation by iron oxides in riparian wetlands, *Chem. Geol.*, 2016, **439**, 161–172.
- 3 E. Lotfi-Kalahroodi, A.-C. Pierson-Wickman, H. Guenet, O. Rouxel, E. Ponzevera, M. Bouhnik-Le Coz, D. Vantelon, A. Dia and M. Davranche, Iron isotope fractionation in iron-organic matter associations: Experimental evidence using filtration and ultrafiltration, *Geochim. Cosmochim. Acta*, 2019, **250**, 98–116.
- 4 G. Ratié, D. Vantelon, E. Lotfi Kalahroodi, I. Bihannic, A. C. Pierson-Wickmann and M. Davranche, Iron speciation at the riverbank surface in wetland and potential impact on the mobility of trace metals, *Sci. Total Environ.*, 2019, **651**, 443–455.
- 5 O. S. Pokrovsky, B. Dupré and J. Schott, Fe–Al–organic Colloids Control of Trace Elements in Peat Soil Solutions: Results of Ultrafiltration and Dialysis, *Aquat. Geochem.*, 2005, **11**, 241–278.
- 6 L. K. ThomasArrigo, C. Mikutta, J. Byrne, K. Barmettler, A. Kappler and R. Kretzschmar, Iron and Arsenic Speciation and Distribution in Organic Flocs from Streambeds of an Arsenic-Enriched Peatland, *Environ. Sci. Technol.*, 2014, **48**, 13218–13228.
- 7 O. S. Pokrovsky and J. Schott, Iron colloids/organic matter associated transport of major and trace elements in small boreal rivers and their estuaries (NW Russia), *Chem. Geol.*, 2002, **190**, 141–179.
- 8 C. Hirst, P. S. Andersson, S. Shaw, I. T. Burke, L. Kutscher, M. J. Murphy, T. Maximov, O. S. Pokrovsky, C.-M. Mörtz and D. Porcelli, Characterisation of Fe-bearing particles and colloids in the Lena River basin, NE Russia, *Geochim. Cosmochim. Acta*, 2017, **213**, 553–573.
- 9 B. Stolpe, L. Guo, A. M. Shiller and G. R. Aiken, Abundance, size distributions and trace-element binding of organic and iron-rich nanocolloids in Alaskan rivers, as revealed by field-flow fractionation and ICP-MS, *Geochim. Cosmochim. Acta*, 2013, **105**, 221–239.
- 10 M. Pédro, A. Dia, M. Davranche, M. Bouhnik-Le Coz, O. Henin and G. Gruau, Insights into colloid-mediated trace element release at the soil/water interface, *J. Colloid Interface Sci.*, 2008, **325**, 187–197.
- 11 C. Mikutta and R. Kretzschmar, Spectroscopic Evidence for Ternary Complex Formation between Arsenate and Ferric Iron Complexes of Humic Substances, *Environ. Sci. Technol.*, 2011, **45**, 9550–9557.
- 12 K. Ritter, G. Aiken R., J. F. Ranville, M. Bauer and D. L. Macalady, Evidence for the Aquatic Binding of Arsenate by Natural Organic Matter–Suspended Fe(III), *Environ. Sci. Technol.*, 2006, **40**, 5380–5387.
- 13 H. Guénet, M. Davranche, D. Vantelon, J. Gigault, S. Prévost, O. Taché, S. Jaksch, M. Pédro, V. Dorcet, A. Boutier and J. Jestin, Characterization of iron–organic matter nano-aggregate networks through a combination of SAXS/SANS and XAS analyses: impact on As binding, *Environ. Sci. Nano*, 2017, **4**, 938–954.
- 14 D. Vantelon, M. Davranche, R. Marsac, C. La Fontaine, H. Guénet, J. Jestin, G. Campaore, A. Beauvois and V. Briois, Iron speciation in iron-organic matter nanoaggregates: A kinetic approach coupling Quick-EXAFS and MCR-ALS chemometry, *Environ. Sci. Nano*, 2019, **6**, 2641–2651.
- 15 T. Karlsson and P. Persson, Coordination chemistry and hydrolysis of Fe(III) in a peat humic acid studied by X-ray absorption spectroscopy, *Geochim. Cosmochim. Acta*, 2010, **74**, 30–40.



- 16 C. Mikutta, X-ray absorption spectroscopy study on the effect of hydroxybenzoic acids on the formation and structure of ferrihydrite, *Geochim. Cosmochim. Acta*, 2011, **75**, 5122–5139. View Article Online  
DOI: 10.1039/D0EN00412J
- 17 M. Pédrot, A. L. Boudec, M. Davranche, A. Dia and O. Henin, How does organic matter constrain the nature, size and availability of Fe nanoparticles for biological reduction?, *J. Colloid Interface Sci.*, 2011, **359**, 75–85.
- 18 C. Chen, J. J. Dynes, J. Wang and D. L. Sparks, Properties of Fe-Organic Matter Associations via Coprecipitation versus Adsorption, *Environ. Sci. Technol.*, 2014, **48**, 13751–13759.
- 19 T. Karlsson and P. Persson, Complexes with aquatic organic matter suppress hydrolysis and precipitation of Fe(III), *Chem. Geol.*, 2012, **322–323**, 19–27.
- 20 L. K. Thomas-Arrigo, J. M. Byrne, A. Kappler and R. Kretzschmar, Impact of Organic Matter on Iron(II)-Catalyzed Mineral Transformations in Ferrihydrite–Organic Matter Coprecipitates, *Environ. Sci. Technol.*, 2018, **52**, 12316–12326.
- 21 C. Mikutta, R. Mikutta, S. Bonneville, F. Wagner, A. Voegelin, I. Christl and R. Kretzschmar, Synthetic coprecipitates of exopolysaccharides and ferrihydrite. Part I: Characterization, *Geochim. Cosmochim. Acta*, 2008, **72**, 1111–1127.
- 22 T. Karlsson, P. Persson, U. Skjellberg, C.-M. Mörtz and R. Giesler, Characterization of Iron(III) in Organic Soils Using Extended X-ray Absorption Fine Structure Spectroscopy, *Environ. Sci. Technol.*, 2008, **42**, 5449–5454.
- 23 S. D. Herzog, L. Gentile, U. Olsson, P. Persson and E. S. Kritzberg, Characterization of Iron and Organic Carbon Colloids in Boreal Rivers and Their Fate at High Salinity, *J. Geophys. Res. Biogeosciences*, 2020, **125**, 1–14.
- 24 U. Schwertmann and R. M. Cornell, Eds., *Iron Oxides in the Laboratory*, Wiley-VCH Verlag GmbH, Weinheim, Germany, 2000.
- 25 J. W. J. van Schaik, I. Persson, D. B. Kleja and J. P. Gustafsson, EXAFS Study on the Reactions between Iron and Fulvic Acid in Acid Aqueous Solutions, *Environ. Sci. Technol.*, 2008, **42**, 2367–2373.
- 26 M. Baalousha, A. Manciuola, S. Cumberland, K. Kendall and J. R. Lead, Aggregation and surface properties of iron oxide nanoparticles: influence of pH and natural organic matter, *Environ. Toxicol. Chem.*, 2008, **27**, 1875.
- 27 M. J. Pullin and S. E. Cabaniss, The effects of pH, ionic strength, and iron–fulvic acid interactions on the kinetics of non-photochemical iron transformations. I. Iron(II) oxidation and iron(III) colloid formation, *Geochim. Cosmochim. Acta*, 2003, **67**, 4067–4077.
- 28 A. Iglesias, R. López, S. Fiol, J. M. Antelo and F. Arce, Analysis of copper and calcium–fulvic acid complexation and competition effects, *Water Res.*, 2003, **37**, 3749–3755.
- 29 A. Ouattmane, M. Hafidi, M. EL Gharous and J. C. Revel, Complexation of calcium ions by humic and fulvic acids, *Analisis*, 1999, **27**, 428–431.
- 30 I. Christl, Ionic strength- and pH-dependence of calcium binding by terrestrial humic acids, *Environ. Chem.*, 2012, **9**, 89.
- 31 A. G. Kalinichev and R. J. Kirkpatrick, Molecular dynamics simulation of cationic complexation with natural organic matter, *Eur. J. Soil Sci.*, 2007, **58**, 909–917.
- 32 J. Adusei-Gyamfi, B. Ouddane, L. Rietveld, J.-P. Cornard and J. Criquet, Natural organic matter-cations complexation and its impact on water treatment: A critical review, *Water Res.*, 2019, **160**, 130–147.
- 33 L. P. Weng, L. K. Koopal, T. Hiemstra, J. C. L. Meeussen and W. H. Van Riemsdijk, Interactions of calcium and fulvic acid at the goethite-water interface, *Geochim. Cosmochim. Acta*, 2005, **69**, 325–339.
- 34 N. Kloster and M. Avena, Interaction of humic acids with soil minerals: adsorption and surface aggregation induced by Ca<sup>2+</sup>, *Environ. Chem.*, 2015, **12**, 731.

- 35 D. Adhikari, T. Sowers, J. W. Stuckey, X. Wang, D. L. Sparks and Y. Yang, Formation and redox reactivity of ferrihydrite-organic carbon-calcium co-precipitates, *Geochim. Cosmochim. Acta*, 2019, **244**, 86–98. View Article Online  
DOI: 10.1039/C9EM00412J
- 36 C. C. Davis and M. Edwards, Role of Calcium in the Coagulation of NOM with Ferric Chloride, *Environ. Sci. Technol.*, 2017, **51**, 11652–11659.
- 37 A.-M. Flank, G. Cauchon, P. Lagarde, S. Bac, M. Janousch, R. Wetter, J.-M. Dubuisson, M. Idir, F. Langlois, T. Moreno and D. Vantelon, LUCIA, a microfocus soft XAS beamline, *Nucl. Instrum. Methods Phys. Res. Sect. B Beam Interact. Mater. At.*, 2006, **246**, 269–274.
- 38 D. Vantelon, N. Trcera, D. Roy, T. Moreno, D. Mailly, S. Guilet, E. Metchalkov, F. Delmotte, B. Lassalle, P. Lagarde and A.-M. Flank, The LUCIA beamline at SOLEIL, *J. Synchrotron Radiat.*, 2016, **23**, 635–640.
- 39 V. Briois, C. La Fontaine, S. Belin, L. Barthe, T. Moreno, V. Pinty, A. Carcy, R. Girardot and E. Fonda, ROCK: the new Quick-EXAFS beamline at SOLEIL, *J. Phys. Conf. Ser.*, 2016, **712**, 012149.
- 40 B. Ravel and M. Newville, *ATHENA*, *ARTEMIS*, *HEPHAESTUS*: data analysis for X-ray absorption spectroscopy using *IFEFFIT*, *J. Synchrotron Radiat.*, 2005, **12**, 537–541.
- 41 E. A. Klop, A. Schouten, P. van der Sluis and A. L. Spek, Structure of calcium acetate monohydrate,  $\text{Ca}(\text{C}_2\text{H}_3\text{O}_2)_2 \cdot \text{H}_2\text{O}$ , *Acta Crystallogr. C*, 1984, **40**, 51–53.
- 42 B. Paluchowska, J. K. Maurin and J. Leciejewicz, Carboxylate and Furan-Ring Oxygen Bonded to Calcium in Polymeric Calcium Furoate, *Acta Crystallogr. C*, 1996, **52**, 347–351.
- 43 M. Newville, EXAFS analysis using *FEFF* and *FEFFIT*, *J. Synchrotron Radiat.*, 2001, **8**, 96–100.
- 44 J. J. Rehr, R. C. Albers and S. I. Zabinsky, High-order multiple-scattering calculations of x-ray-absorption fine structure, *Phys. Rev. Lett.*, 1992, **69**, 3397–3400.
- 45 A. Radulescu, N. K. Szekely and M.-S. Appavou, KWS-2: Small angle scattering diffractometer, *J. Large-Scale Res. Facil. JLSRF*, 2015, **1**, A29.
- 46 V. Pipich and Z. Fu, KWS-3: Very small angle scattering diffractometer with focusing mirror, *J. Large-Scale Res. Facil. JLSRF*, 2015, **1**, A31.
- 47 B. Hammouda, A new Guinier–Porod model, *J. Appl. Crystallogr.*, 2010, **43**, 716–719.
- 48 J. Dubochet and A. W. McDowell, Vitrification of pure water for electron microscopy, *J. Microsc.*, 1981, **124**, 3–4.
- 49 A. Sorrentino, J. Nicolás, R. Valcárcel, F. J. Chichón, M. Rosanes, J. Avila, A. Tkachuk, J. Irwin, S. Ferrer and E. Pereiro, MISTRAL: a transmission soft X-ray microscopy beamline for cryo nano-tomography of biological samples and magnetic domains imaging, *J. Synchrotron Radiat.*, 2015, **22**, 1112–1117.
- 50 J. Otón, C. O. S. Sorzano, R. Marabini, E. Pereiro and J. M. Carazo, Measurement of the modulation transfer function of an X-ray microscope based on multiple Fourier orders analysis of a Siemens star, *Opt. Express*, 2015, **23**, 9567.
- 51 M. Wilke, F. Farges, P.-E. Petit, G. E. Brown and F. Martin, Oxidation state and coordination of Fe in minerals: An Fe K- XANES spectroscopic study, *Am. Mineral.*, 2001, **86**, 714–730.
- 52 C. Chen and A. Thompson, Ferrous Iron Oxidation under Varying  $\text{pO}_2$  Levels: The Effect of Fe(III)/Al(III) Oxide Minerals and Organic Matter, *Environ. Sci. Technol.*, 2018, **52**, 597–606.
- 53 A. Vilgé-Ritter, J. Rose, A. Masion, J.-Y. Bottero and J.-M. Lainé, Chemistry and structure of aggregates formed with Fe-salts and natural organic matter, *Colloids Surf. Physicochem. Eng. Asp.*, 1999, **147**, 297–308.
- 54 F. M. Michel, L. Ehm, G. Liu, W. Q. Han, S. M. Antao, P. J. Chupas, P. L. Lee, K. Knorr, H. Eulert, J. Kim, C. P. Grey, A. J. Celestian, J. Gillow, M. A. A. Schoonen, D. R. Strongin and J. B. Parise, Similarities in 2- and 6-Line Ferrihydrite Based on Pair Distribution Function Analysis of X-ray Total Scattering, *Chem. Mater.*, 2007, **19**, 1489–1496.



- 55 E. Neubauer, W. D. C. Schenkeveld, K. L. Plathe, C. Rentenberger, F. von der Kammer, S. M. Kraemer and T. Hofmann, The influence of pH on iron speciation in podzol extracts: Iron complexes with natural organic matter, and iron mineral nanoparticles, *Sci. Total Environ.*, 2013, **461–462**, 108–116.
- 56 H. P. Jarvie and S. M. King, Small-Angle Neutron Scattering Study of Natural Aquatic Nanocolloids, *Environ. Sci. Technol.*, 2007, **41**, 2868–2873.
- 57 S. M. King and H. P. Jarvie, Exploring How Organic Matter Controls Structural Transformations in Natural Aquatic Nanocolloidal Dispersions, *Environ. Sci. Technol.*, 2012, **46**, 6959–6967.
- 58 M. S. Diallo, C. J. Glinka, W. A. Goddard and J. H. Johnson, Characterization of nanoparticles and colloids in aquatic systems 1. Small angle neutron scattering investigations of Suwannee River fulvic acid aggregates in aqueous solutions, *J. Nanoparticle Res.*, 2005, **7**, 435–448.
- 59 R. Osterberg and K. Mortensen, Fractal dimension of humic acids: A small angle neutron scattering study, *Eur. Biophys. J.*, 1992, **21**, 163–167.
- 60 R. Osterberg and K. Mortensen, The growth of fractal humic acids: Cluster correlation and gel formation, *Radiat. Environ. Biophys.*, 1994, **33**, 269–276.
- 61 V. Martin-Diaconescu, M. Gennari, B. Gerey, E. Tsui, J. Kanady, R. Tran, J. Pécaut, D. Maganas, V. Krewald, E. Gouré, C. Duboc, J. Yano, T. Agapie, M.-N. Collomb and S. DeBeer, Ca K-Edge XAS as a Probe of Calcium Centers in Complex Systems, *Inorg. Chem.*, 2015, **54**, 1283–1292.
- 62 J. L. Fulton, S. M. Heald, Y. S. Badyal and J. M. Simonson, Understanding the Effects of Concentration on the Solvation Structure of  $\text{Ca}^{2+}$  in Aqueous Solution. I: The Perspective on Local Structure from EXAFS and XANES, *J. Phys. Chem. A*, 2003, **107**, 4688–4696.
- 63 D. Graf, Crystallographic Tables for the Rhombohedral Carbonates, *Am. Mineral.*, 1961, **46**, 1283–1316.
- 64 T. D. Sowers, D. Adhikari, J. Wang, Y. Yang and D. L. Sparks, Spatial Associations and Chemical Composition of Organic Carbon Sequestered in Fe, Ca, and Organic Carbon Ternary Systems, *Environ. Sci. Technol.*, 2018, **52**, 6936–6944.
- 65 E. Iskrenova-Tchoukova, A. G. Kalinichev and R. J. Kirkpatrick, Metal Cation Complexation with Natural Organic Matter in Aqueous Solutions: Molecular Dynamics Simulations and Potentials of Mean Force, *Langmuir*, 2010, **26**, 15909–15919.
- 66 R. Kretzschmar and T. Schäfer, Metal Retention and Transport on Colloidal Particles in the Environment, *Elements*, 2005, **1**, 205–210.
- 67 J. D. Ritchie and E. M. Perdue, Proton-binding study of standard and reference fulvic acids, humic acids, and natural organic matter, *Geochim. Cosmochim. Acta*, 2003, **67**, 85–96.
- 68 M. Auffan, J. Rose, O. Proux, D. Borschneck, A. Masion, P. Chaurand, J.-L. Hazemann, C. Chaneac, J.-P. Jolivet, M. R. Wiesner, A. Van Geen and J.-Y. Bottero, Enhanced Adsorption of Arsenic onto Maghemite Nanoparticles: As(III) as a Probe of the Surface Structure and Heterogeneity, *Langmuir*, 2008, **24**, 3215–3222.
- 69 O. S. Pokrovsky, L. S. Shirokova, S. N. Kirpotin, S. Audry, J. Viers and B. Dupré, Effect of permafrost thawing on organic carbon and trace element colloidal speciation in the thermokarst lakes of western Siberia, *Biogeosciences*, 2011, **8**, 565–583.

## Table of contents entry

Calcium drives the structural transitions of iron-organic matter associations from colloidal aggregates to a non-colloidal micrometric network, subsequently controlling their mobility and the iron surface reactivity.

